Section 3.2

Statistical Properties: The Hipparcos Catalogue

3.2. Statistical Properties: The Hipparcos Catalogue

In this section statistical properties of data from the Hipparcos Catalogue are presented, mainly in the form of distributions over the sky, and frequency histograms. In most cases data from the Catalogue have been used directly; in a few cases it was considered appropriate to apply certain transformations in order to demonstrate a physical or astrometric effect. In particular this involves the transformation to the ecliptic and galactic coordinate systems.

3.2.1. Density of Observed Stars

The density of observed stars in the Hipparcos Catalogue depends strongly on the galactic latitude. Within the galactic plane, maxima of the density occur around $l = 100°$ and $l = 300°$, as shown in Figures 3.2.1 and 3.2.2. These maxima are related to the position of the Orion arm of our Galaxy, and the Gould Belt (at $l = 270°$). Noteworthy is also the concentration around $l = 200°$, $b = -20°$, the position of the Orion associations. The area around $l = 15°$, $b = 15°$ with low density corresponds to the dark nebula in Ophiuchus.

The number of observed stars per ecliptic latitude range and per magnitude class is given in Table 3.2.1. The maxima in the range $50° < |\beta| < 60°$ are a direct consequence of the distribution in the galactic plane.

Table 3.2.1. The number of entries in the Hipparcos Catalogue with associated astrometry, divided according to ecliptic latitude (β) and magnitude (median magnitude, *Hp*, from Field H44).

	Ecliptic latitude ($\|\beta\|$, deg)								
Hp	0–10	10–20	20–30	30–40	40–50	50–60	60–70	70–90	0–90
<2	7	7	6	6	8	6	3	3	46
2–3	21	20	21	11	19	15	8	4	119
3–4	53	45	55	34	40	42	24	22	315
4–5	165	150	152	128	140	121	79	56	991
5–6	490	444	459	420	394	401	281	199	3088
6–7	1434	1365	1457	1345	1241	1156	841	542	9381
7–8	3494	3408	3538	3416	3304	3048	2055	1416	23679
8–9	5895	5842	6015	6006	5909	4814	3566	2682	40729
9–10	4038	4237	4362	4091	4189	3201	2239	1556	27913
10–11	1212	1426	1735	1405	1198	791	460	336	8563
11–12	397	400	407	380	360	294	134	129	2501
≥12	105	120	79	112	76	65	38	35	630
all	17311	17464	18286	17354	16878	13954	9728	6980	117955

3.2.2. Great-Circle Abscissae

The distribution of the median number of great-circle abscissae used for the determination of the astrometric parameters of each catalogue entry is shown in Figure 3.2.3. The numbers used for the construction of this graph are the averages of the number of great-circle abscissae employed by the FAST and NDAC consortia. These numbers are, by nature, closely related to the number of (accepted) photometric transits, for which results are given in Figure 3.2.87. An important difference is that the observations obtained during sun-pointing periods (cf. Volume 3, Chapter 2) are included here. Sun-pointing observations were included in the astrometric adjustments, but the corresponding photometric transits were not considered acceptable (cf. Section 2.5, Field HH5). Traces of the extended sun-pointing period near the end of the mission (around 1 January 1993) are visible at $\lambda \sim 10°$ and $\lambda \sim 190°$; there are also fainter tracks due to shorter sun-pointing episodes in October 1991 ($\lambda \sim 105°$ and $\lambda \sim 285°$) and in August 1992 ($\lambda \sim 60°$ and $\lambda \sim 240°$). The remaining structure in this graph is explained in detail by the definition of the Hipparcos scanning law, the measurement interruptions, and the duration of the mission.

In Section 2.1, under Field H29, an approximate relation is given between the accepted number of transits and the number of great-circle abscissae (quoting a factor of 3.55). This relation is valid for the majority of catalogue entries. In reality, the factor increases for higher numbers of transits. The median number of astrometric abscissae as a function of the number of accepted photometric transits is given in Figure 3.2.4. Note that the higher numbers of transits (> 150) occur only for a small fraction of stars (cf. Figure 3.2.88).

3.2.3. Parallaxes and Proper Motions

The sky distribution of median parallaxes is given in Figure 3.2.5. The frequency histogram is in Figure 3.2.6. The parallaxes are systematically lower in the galactic plane. In a flattened system like the Galaxy, stars are expected to lie further away in the plane. The Hipparcos horizon is well beyond half the thickness of the galactic disk. In Figure 3.2.7 the distributions of parallaxes within and outside the galactic plane are compared.

Systematically larger parallaxes are found in the Hyades region (about 210 members of this open cluster were included in the Hipparcos Input Catalogue), and in the dark nebula region in Ophiuchus where in some places the view beyond 250 pc is obstructed. Distributions of the parallaxes in these two regions can be found in Figure 3.2.8.

The proper motions (Figures 3.2.9 to 3.2.12) show a systematic effect linked to the apex motion of the solar system with respect to the local standard of rest (velocity about 16.5 km/s) towards the point $l = 53°$, $b = 25°$, or $\alpha \sim 270°$, $\delta \sim 30°$. In order to demonstrate this effect more distinctly, Figures 3.2.13 to 3.2.14 give the transverse velocities (cf. Equation 1.2.20) for stars with a parallax greater than 7.5 mas. The systematic trends in these figures again reflect the motion of the solar system with respect to the local standard of rest.

3.2.4. Standard Errors and Correlations

The astrometric standard errors and correlations are given in the Catalogue in the equatorial coordinate system. The Hipparcos scanning strategy was, however, defined with respect to the sun position; as a consequence the error properties of the results are more readily understood in terms of ecliptic coordinates. For this reason the results for these parameters are presented here in both coordinate systems.

Sky distributions of the standard errors of the five astrometric parameters are shown in Figures 3.2.15, 3.2.19, 3.2.23, 3.2.29, and 3.2.33 in the equatorial coordinate system, and in Figures 3.2.16, 3.2.20, 3.2.24, 3.2.30, and 3.2.34 in the ecliptic coordinate system. Frequency distributions of these standard errors are given in Figures 3.2.18, 3.2.22, 3.2.26, 3.2.32, and 3.2.36. The dependence of the standard errors on ecliptic latitude is in Figures 3.2.17, 3.2.21, 3.2.25, 3.2.31, and 3.2.35, and the dependence of the standard errors on the *Hp* magnitude is in Figures 3.2.37, 3.2.38, 3.2.39, 3.2.40, and 3.2.41. The values of the standard errors for each of the five astrometric parameters per ecliptic latitude range and per magnitude class are given in Tables 3.2.2 to 3.2.6.

All these standard errors depend on ecliptic latitude. This is a direct consequence of the Hipparcos scanning strategy, wherein scanning circles must have a minimum angle of 47° with the ecliptic. This had two effects: stars with ecliptic latitude $|\beta| \geq 47°$ were observed more frequently than the stars closer to the ecliptic (with a marked maximum at $|\beta| = 47°$, cf. also Figures 3.2.88 and 3.2.89), and the latter stars were preferentially scanned in directions perpendicular to the ecliptic, thereby leading to a considerably better determination of the latitude components of the parameters. For the longitudinal components of the astrometric parameters these effects cooperate and explain the strong dependence on ecliptic latitude, whereas for the latitudinal components the effects work in opposite directions, so that a less pronounced effect in ecliptic latitude may be expected. In the region around $|\beta| = 47°$ there is an emphasis on longitudinal measurements; minimum values of the standard errors of $\lambda*$ and $\mu_{\lambda*}$ (and consequently $\alpha*$ and $\mu_{\alpha*}$) are found there.

Sky distributions for the relative precision of the distance σ_π/π are given in Figures 3.2.27 and 3.2.28. The structure is mainly related to the precision of the parallax. There is a conspicuous systematic effect of less precise distances around the galactic meridians $l = 0°$ and $l = 180°$. This systematic effect is the direct consequence of the decision to include extra F and G stars near the galactic meridian plane through the galactic centre and anticentre in the Hipparcos Input Catalogue (cf. ESA SP-1111, Vol. 2, Section 7.3). A related effect appears in a number of photometric results.

The distributions over the sky of the various correlations, in ecliptic and equatorial coordinates, are shown in Figures 3.2.42 to 3.2.61. Frequency histograms for the ten correlations in the equatorial coordinate system are in Figure 3.2.66.

One of the consequences of using the equatorial coordinate system is the introduction of certain systematic effects in some of the astrometric correlations. For example, the axes of the error ellipses of λ versus β tend to be parallel to the ecliptic latitude circles, i.e. the connected correlations are low. Transforming to the equatorial system introduces a rotation over an angle dependent on the position on the sky, and therefore a position-dependent correlation. The size of this correlation depends on the rotation angle between the local plane coordinate systems (cf. Sections 1.2.9 and 1.5.3) in equatorial and ecliptic coordinates, respectively, and on the eccentricity of the error ellipse, in other words, the difference between $\sigma_{\lambda*}$ and σ_β. In the region around the

Table 3.2.2. Median standard errors in right ascension, $\sigma_{\alpha*}$, for the entries in the Hipparcos Catalogue with associated astrometry, divided according to ecliptic latitude and magnitude as in Table 3.2.1, and expressed in milliarcsec (mas) for the catalogue epoch J1991.25.

	Ecliptic latitude ($\|\beta\|$, deg)								
Hp	0–10	10–20	20–30	30–40	40–50	50–60	60–70	70–90	0–90
<2	0.80	0.90	0.71	0.60	0.43	0.46	0.48	0.50	0.69
2–3	0.87	0.73	0.69	0.58	0.39	0.41	0.42	0.44	0.65
3–4	0.81	0.75	0.69	0.58	0.42	0.42	0.44	0.47	0.63
4–5	0.80	0.75	0.68	0.59	0.41	0.42	0.44	0.48	0.63
5–6	0.80	0.75	0.68	0.57	0.41	0.42	0.44	0.46	0.62
6–7	0.83	0.79	0.72	0.61	0.45	0.45	0.47	0.49	0.65
7–8	0.92	0.89	0.82	0.70	0.53	0.52	0.54	0.55	0.73
8–9	1.08	1.04	0.97	0.83	0.65	0.64	0.65	0.66	0.86
9–10	1.33	1.28	1.19	1.02	0.82	0.79	0.80	0.79	1.07
10–11	1.80	1.73	1.60	1.37	1.14	1.10	1.05	1.04	1.51
11–12	2.64	2.54	2.39	2.04	1.70	1.61	1.62	1.58	2.22
≥12	3.92	3.64	3.50	3.32	3.12	2.52	3.27	2.39	3.45
all	1.11	1.08	1.01	0.86	0.67	0.65	0.66	0.66	0.87

Table 3.2.3. Median standard errors in declination, σ_δ, for the entries in the Hipparcos Catalogue with associated astrometry, divided according to ecliptic latitude and magnitude as in Table 3.2.1, and expressed in milliarcsec (mas) for the catalogue epoch J1991.25.

	Ecliptic latitude ($\|\beta\|$, deg)								
Hp	0–10	10–20	20–30	30–40	40–50	50–60	60–70	70–90	0–90
<2	0.53	0.60	0.46	0.49	0.45	0.47	0.42	0.46	0.49
2–3	0.59	0.52	0.51	0.49	0.46	0.44	0.44	0.45	0.50
3–4	0.55	0.53	0.53	0.52	0.44	0.44	0.42	0.45	0.48
4–5	0.54	0.52	0.52	0.50	0.44	0.44	0.43	0.44	0.48
5–6	0.53	0.52	0.51	0.48	0.45	0.44	0.43	0.45	0.48
6–7	0.55	0.55	0.54	0.52	0.49	0.48	0.47	0.48	0.51
7–8	0.61	0.61	0.60	0.59	0.57	0.56	0.54	0.54	0.58
8–9	0.72	0.72	0.72	0.71	0.71	0.69	0.66	0.65	0.70
9–10	0.89	0.89	0.89	0.88	0.90	0.85	0.81	0.80	0.87
10–11	1.21	1.21	1.20	1.17	1.21	1.17	1.07	1.06	1.18
11–12	1.82	1.82	1.80	1.77	1.85	1.71	1.58	1.60	1.78
≥12	2.73	2.61	2.66	2.72	3.04	2.86	3.11	2.37	2.69
all	0.74	0.75	0.75	0.73	0.74	0.69	0.66	0.66	0.72

Table 3.2.4. Median standard errors in parallax, σ_π, for the entries in the Hipparcos Catalogue with associated astrometry, divided according to ecliptic latitude and magnitude as in Table 3.2.1, and expressed in milliarcsec (mas).

	Ecliptic latitude ($\|\beta\|$, deg)								
Hp	0–10	10–20	20–30	30–40	40–50	50–60	60–70	70–90	0–90
<2	0.88	0.98	0.90	0.78	0.64	0.60	0.53	0.49	0.79
2–3	0.88	0.81	0.77	0.76	0.68	0.56	0.49	0.48	0.76
3–4	0.91	0.82	0.79	0.74	0.65	0.55	0.52	0.49	0.74
4–5	0.88	0.86	0.81	0.76	0.66	0.55	0.51	0.48	0.75
5–6	0.88	0.85	0.82	0.75	0.67	0.56	0.52	0.49	0.75
6–7	0.92	0.90	0.86	0.81	0.73	0.61	0.55	0.52	0.80
7–8	1.02	1.01	0.97	0.92	0.86	0.72	0.63	0.59	0.91
8–9	1.21	1.19	1.16	1.12	1.07	0.89	0.77	0.71	1.09
9–10	1.49	1.47	1.43	1.37	1.35	1.11	0.94	0.86	1.36
10–11	2.01	1.97	1.93	1.82	1.84	1.54	1.24	1.13	1.85
11–12	2.98	2.96	2.81	2.74	2.73	2.26	1.88	1.73	2.72
≥12	4.35	4.19	4.11	4.10	4.00	3.67	3.49	2.51	4.11
all	1.23	1.24	1.20	1.15	1.11	0.89	0.77	0.71	1.10

ecliptic equator, $\sigma_{\lambda*} > \sigma_\beta$, and a sinusoidal variation along the ecliptic is expected. Around $|\beta| = 47°$, $\sigma_{\lambda*}$ becomes rather abruptly smaller than σ_β, leading to an inversion in the sign of the transformed correlation. In the ecliptic pole region, $\sigma_{\lambda*} \sim \sigma_\beta$; no systematic effect is expected. All these features are clearly discernible in Figure 3.2.42.

Other systematic features can be ascribed to non-uniform coverage due to the effects of the measurement interruptions (see Volume 2, Section 7.3). Measurements on stars that are asymmetrically distributed with respect to the epoch of the catalogue are expected to exhibit correlations between position and proper motion components ($\alpha*$, $\mu_{\alpha*}$) and (δ, μ_δ) and their analogues in ecliptic coordinates. Figure 3.2.62 gives the results for the mean epoch of observation computed from individual measurement epochs, and agrees very well with the results for the relevant correlations. In Section 1.2.7 the definition of an effective mean epoch computed from the correlation coefficients is given (Equation 1.2.10). Its sky distribution is given for comparison in Figure 3.2.63. In the same section (Equations 1.2.6 and 1.2.8) a definition of the effective mean epochs for right ascension and declination is given. The distribution of the difference between these epochs is shown in Figure 3.2.65. The time span over which observations were made also varies considerably over the sky (Figure 3.2.64). This explains the larger standard errors obtained in some unfavourably covered regions.

There are two more systematic effects to be discussed: one is an asymmetry in the distribution of the correlation between parallax and declination, visible mainly in the histogram (Figure 3.2.66), but also in the sky distribution (Figure 3.2.46). The negative mean value for this correlation is a consequence of the scanning law. The nominal scanning law is defined such that the speed of the nominal z-axis relative to the stars is roughly constant. Because the revolving motion about the sun was chosen in the clockwise direction, as seen from the satellite, this means that the z-axis must spend more time south of the ecliptic than on the north side. When the z-axis is directly below the sun ($\nu = 270°$, see Chapter 8 of Volume 2), the latitude component of the

Table 3.2.5. Median standard errors of proper motion in right ascension, $\sigma_{\mu_{\alpha*}}$, for the entries in the Hipparcos Catalogue with associated astrometry, divided according to ecliptic latitude and magnitude as in Table 3.2.1, and expressed in milliarcsec per year (mas/yr).

	Ecliptic latitude ($\|\beta\|$, deg)								
Hp	0–10	10–20	20–30	30–40	40–50	50–60	60–70	70–90	0–90
<2	1.02	0.99	0.76	0.59	0.53	0.54	0.54	0.53	0.72
2–3	1.02	0.84	0.78	0.64	0.48	0.44	0.46	0.46	0.74
3–4	1.02	0.88	0.81	0.64	0.46	0.49	0.48	0.52	0.67
4–5	0.94	0.90	0.80	0.66	0.47	0.48	0.49	0.50	0.69
5–6	0.95	0.89	0.80	0.67	0.47	0.48	0.51	0.51	0.68
6–7	1.00	0.95	0.84	0.72	0.53	0.52	0.54	0.54	0.73
7–8	1.10	1.07	0.96	0.82	0.62	0.60	0.62	0.61	0.83
8–9	1.31	1.26	1.16	0.99	0.77	0.74	0.75	0.73	0.99
9–10	1.63	1.56	1.45	1.22	0.98	0.94	0.93	0.90	1.26
10–11	2.23	2.16	1.96	1.66	1.36	1.31	1.25	1.19	1.80
11–12	3.29	3.19	2.91	2.46	2.05	1.98	1.92	1.72	2.67
≥12	5.02	4.63	4.23	4.05	3.22	3.04	3.72	2.72	4.25
all	1.34	1.31	1.20	1.02	0.79	0.75	0.75	0.74	1.02

Table 3.2.6. Median standard errors of proper motion in declination, σ_{μ_δ}, for the entries in the Hipparcos Catalogue with associated astrometry, divided according to ecliptic latitude and magnitude as in Table 3.2.1, and expressed in milliarcsec per year (mas/yr).

	Ecliptic latitude ($\|\beta\|$, deg)								
Hp	0–10	10–20	20–30	30–40	40–50	50–60	60–70	70–90	0–90
<2	0.57	0.62	0.47	0.53	0.49	0.55	0.43	0.45	0.54
2–3	0.68	0.61	0.62	0.56	0.56	0.49	0.47	0.52	0.59
3–4	0.70	0.62	0.63	0.61	0.50	0.51	0.47	0.54	0.58
4–5	0.64	0.64	0.62	0.57	0.51	0.48	0.49	0.51	0.56
5–6	0.66	0.62	0.60	0.56	0.52	0.50	0.49	0.53	0.56
6–7	0.67	0.66	0.63	0.61	0.56	0.54	0.53	0.56	0.60
7–8	0.75	0.75	0.72	0.69	0.66	0.64	0.61	0.64	0.68
8–9	0.89	0.88	0.87	0.83	0.82	0.78	0.75	0.77	0.83
9–10	1.10	1.10	1.08	1.02	1.04	0.99	0.94	0.96	1.03
10–11	1.54	1.51	1.44	1.36	1.44	1.37	1.23	1.28	1.42
11–12	2.28	2.27	2.11	2.12	2.13	1.98	1.86	1.90	2.12
≥12	3.53	3.34	3.12	3.11	3.44	3.58	3.83	3.05	3.33
all	0.90	0.91	0.89	0.86	0.85	0.79	0.75	0.78	0.85

parallactic displacement on the scanning circle is negative for all stars along the circle. Conversely, when the z-axis is above the sun ($\nu = 90°$), the parallax has a positive latitude component. Since the former situation occurs during a longer time interval than the latter, it follows that the parallax on average has a negative latitude component, and therefore that the mean correlation between the parallax and the latitude is negative. A nominal scanning law chosen such that the revolving motion was counterclockwise as seen from the satellite would have resulted in a positive mean correlation. (Of the 2328 reference great circles in the N37.05 solution, cf. Chapter 16 of Volume 3, 1273, or 55 per cent, have poles with a negative declination.)

The other systematic effect is the global variation of the correlations between right ascension and parallax (and to a lesser extent, those between proper motion in right ascension and parallax). In order to obtain a low correlation between ecliptic longitude and parallax, the measurements should be symmetrically distributed over the ellipse described by the parallactic motion. In particular, for a star on the ecliptic, equal numbers of measurements should be obtained on both sides of the sun. In the case of Hipparcos, this condition is not fulfilled: for the actual mission interval, observations were made in all four years between January and March, whereas the period from September to November was covered only twice. This explains a global systematic effect ranging from +0.4 to −0.4; within this global variation, much faster variations are seen, related to the presence or absence of particular scanning circles during these periods. The traces of these scanning circles are clearly visible in the plot, Figure 3.2.45.

Figures 3.2.67 to 3.2.70 give results for the indicators of solution quality F1 and F2. Occasional higher rejection rates are mainly found in the region around the ecliptic; the rejection percentages appear to be slightly higher systematically in the ecliptic pole regions. These patterns are essentially a quantisation effect: for, say, 30 abscissae the rejection of one abscissa gives a rejection percentage of 3 without the possibility for values between 0 and 3. The values for F2, the goodness-of-fit indicator, are systematically higher in the region of the ecliptic than in the ecliptic pole regions, indicating a slightly less satisfactory adjustment in general.

3.2.5. Photometric Data

Figures 3.2.71 to 3.2.74 give frequency distributions for the Tycho B_T and V_T magnitudes and their associated standard errors.

The distribution of colours over the sky is shown in Figure 3.2.75 for the $B - V$ colour index and in Figure 3.2.77 for the $V - I$ colour index. In the galactic plane more early-type stars are observed than elsewhere. The young stars in the Orion associations stand out at $l = 200°$, $b = -20°$. The bands of slightly bluer stars at $l = 0°$ and $l = 180°$ are a consequence of the already mentioned selection of extra F and G stars near the galactic meridian plane through the galactic centre and anticentre for the Hipparcos Input Catalogue.

The frequency distribution of both colour indices are given in Figures 3.2.76 and 3.2.78 and show similar features. The peak around $B - V = 0$ mag is due to the inclusion, in the Hipparcos Input Catalogue, of a large number of early-type stars for galactic structure studies. The high peak near $B - V = 0.5$ mag is due to the survey stars near the turn-off (cf. also the Hertzsprung-Russell diagrams in Section 3.5), indicating that the mean age of the galactic disk is about $5\,10^9$ yr. The maximum around $B - V = 1$ mag is due to

the G8–K0 giants in the core helium burning phase. The small bump in the interval $B - V = 1.3 - 1.7$ mag is due to nearby dK–dM dwarfs.

Frequency distributions of the standard errors for the colour indices are given in Figures 3.2.79 and 3.2.80.

The sky distribution of the magnitude in the Hipparcos photometric system *Hp* is displayed in Figure 3.2.81. The special selection for $l = 0°$ and $l = 180°$ mentioned before manifests itself here as the presence of fainter stars in these areas. There are further global variations over the sky. The frequency distribution is given in Figure 3.2.82. The associated standard error is found in Figures 3.2.83 and 3.2.84.

The scatter in the photometric observations (cf. Section 1.3, Appendix 1) is shown in Figures 3.2.85 and 3.2.86. There is a clear enhancement in the regions around $|\beta| = 47°$, where the number of observation is greatest (see below). It can be shown that the value of the scatter is correlated with the number of observations in the Hipparcos Catalogue.

The distributions of the number of accepted photometric transits (also a measure of the number of astrometric measurements, see Section 3.2.2) are shown in three different representations in Figures 3.2.87, 3.2.88, and 3.2.89. The structure of these plots follows accurately from the Hipparcos scanning law and the limited duration of the mission. Note that the periods of sun pointing leave no trace in these diagrams because they do not yield any accepted photometric transits. The two peaks in the histogram correspond to observations in the regions $|\beta| < 47°$ and $|\beta| > 47°$, respectively.

The sky distribution of the median amplitude of luminosity variations is given in Figure 3.2.90. As was the case for the scatter, enhanced values are found around $|\beta| = 47°$. In the Hipparcos Catalogue, there is a correlation between the number of photometric transits and the amplitude. This has not been studied in detail, but evidently the probability of detecting variability increases with the number of observations.

Frequency distributions for various other results from the photometric analysis are presented in Figures 3.2.91 to 3.2.97. Figure 3.2.97 deserves some explanation (cf. Volume 3, Section 21.4). The broad peak below 10 days corresponds to the region where the spacing of Hipparcos observations is optimally suited to determine periods. It is in this region that most newly-discovered periods are found. The other peak around 250 days indicates the period range where Hipparcos can confirm and possibly improve already known periods (the distribution of longer gaps between observations peaks between 85 and 140 days at lower ecliptic latitudes, cf. Volume 3, Figure 14.16).

3.2.6. Multiple-Star Data

Results for the multiple-star data as given in the main catalogue are presented in Figures 3.2.98 to 3.2.106, mostly in the form of frequency histograms. These plots illustrate the absence of significant systematic effects in the detection and characterisation of double systems. There appears to be a slight preference for larger magnitude differences in the galactic plane, perhaps related to the brighter stars in that region (Figure 3.2.102). The diagram of separation versus magnitude difference (Figure 3.2.106) shows, not unexpectedly, that for the detection of larger differences in magnitude larger separations are needed. The upper limit at 10 arcsec corresponds to the typical changeover to

two-pointing systems for *a priori* known doubles (cf. Section 1.4.2). Components were sometimes detected beyond this separation limit, especially for larger differences in magnitude.

Results from the Double and Multiple Systems Annex (DMSA) are organised according to the various solution types.

Results from the DMSA, Acceleration Solutions (DMSA/G) are given in Figures 3.2.107 to 3.2.112. The cut-offs in Figures 3.2.109 and 3.2.112 for values below 3.44 are a consequence of the choice of the limit for significance of the acceleration solutions (Section 2.3.1). The entries present below this limit for F_g have a significant $F_{\dot{g}}$.

Results from the DMSA, Orbital Solutions (DMSA/O) are presented in Figures 3.2.113 to 3.2.119. Not unexpectedly, Hipparcos measurements are optimal for the determination of orbital periods of a few years (Figure 3.2.113). In the absence of spectroscopic information there is an ambiguity of $\pm 180°$ in the position angle of the ascending node, in which case the catalogue gives the value between $0°$ and $180°$. This explains why in Figure 3.2.119 there are more entries in the first two quadrants than in the other two.

Results from the DMSA, Variability-Induced Mover (VIM) Solutions (DMSA/V) are in Figures 3.2.120 to 3.2.125. The distributions for the parameters from the DMSA, Stochastic Solutions (DMSA/X) are in Figures 3.2.126 and 3.2.127.

Figure 3.2.1. *Hipparcos Catalogue: number of observed stars per square degree, in galactic coordinates (cell size $2^\circ \times 2^\circ$). On the average there are 2.8 stars per square degree in the Hipparcos Catalogue.*

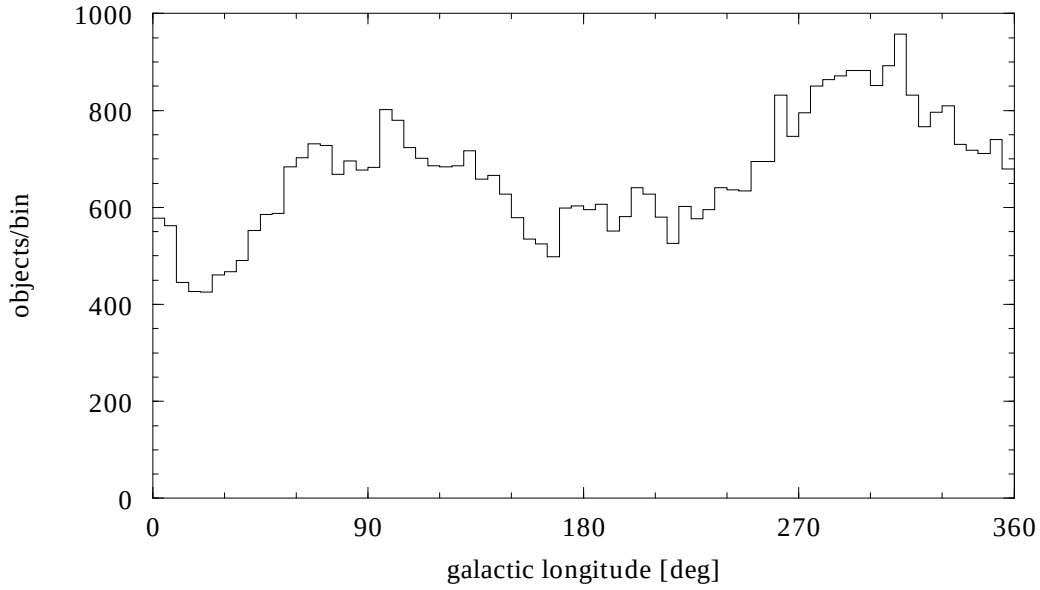

Figure 3.2.2. *Distribution of number of stars near the galactic equator ($|b| < 10^\circ$, bin size 5°).*

Figure 3.2.3. *Hipparcos Catalogue: median number of great-circle abscissae used for astrometry, in ecliptic coordinates (cell size $2° \times 2°$).*

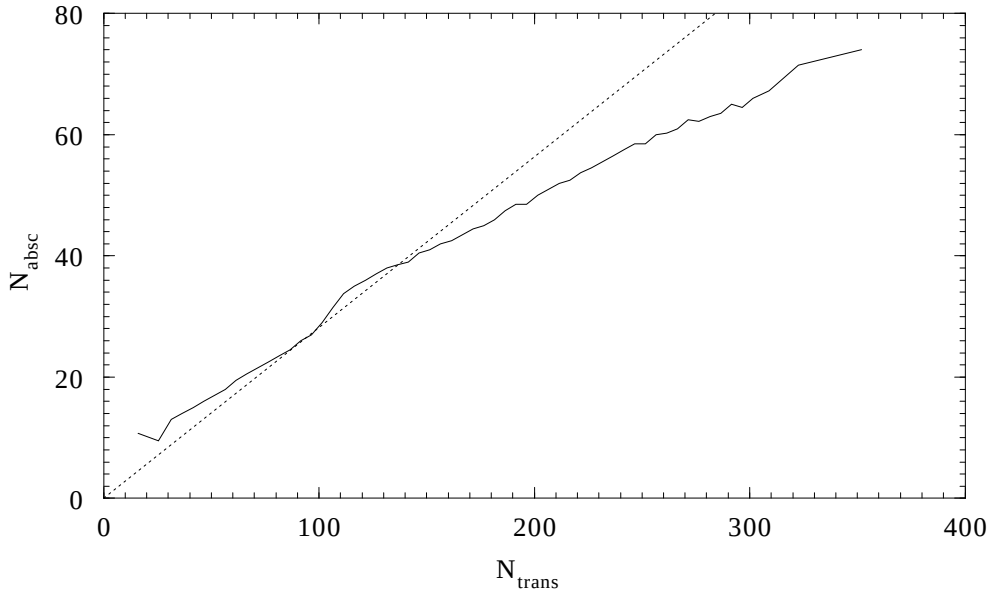

Figure 3.2.4. *Hipparcos Catalogue: median number of abscissae used for astrometry versus number of accepted photometric transits. The dotted line represents the approximate relation valid for most entries, as given in Section 2.1, under Field H29.*

Figure 3.2.5. *Hipparcos Catalogue, Field H11: median parallax π, in galactic coordinates (cell size $2° \times 2°$). On the average the stars of the Hipparcos Catalogue are more distant in the galactic plane than outside this plane.*

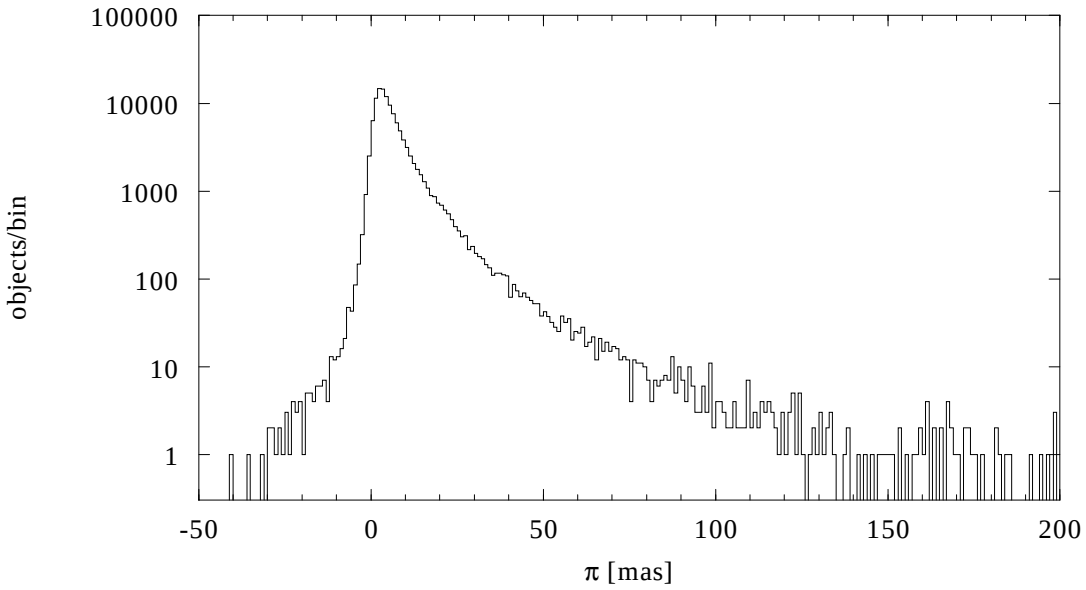

Figure 3.2.6. *Hipparcos Catalogue, Field H11: parallax π (bin size 1 mas).*

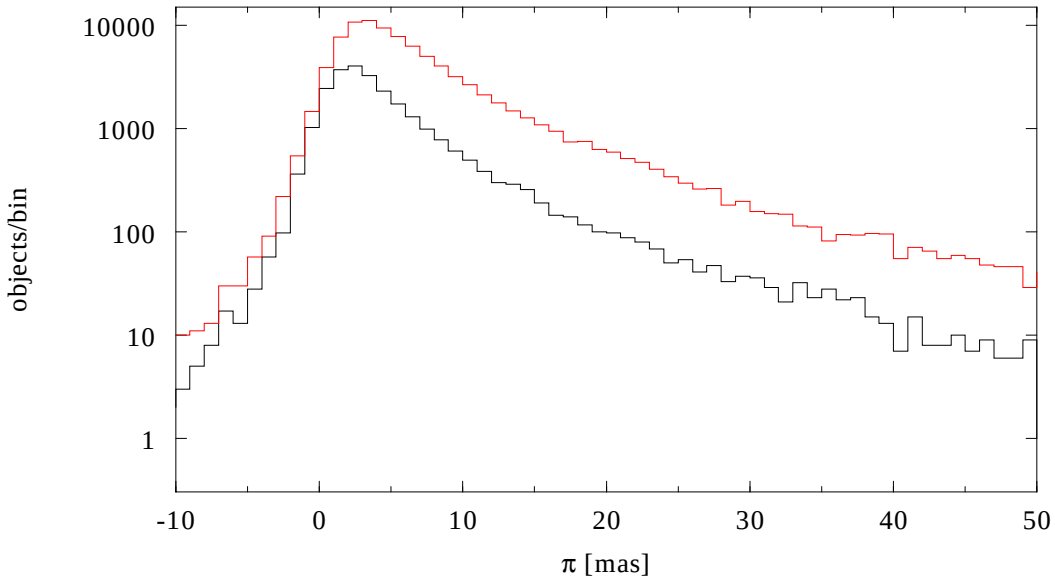

Figure 3.2.7. *Distribution of parallaxes within and outside the galactic plane (bin size 1 mas). Black line: stars with* $|b| < 10°$. *Red line: stars with* $|b| \geq 10°$.

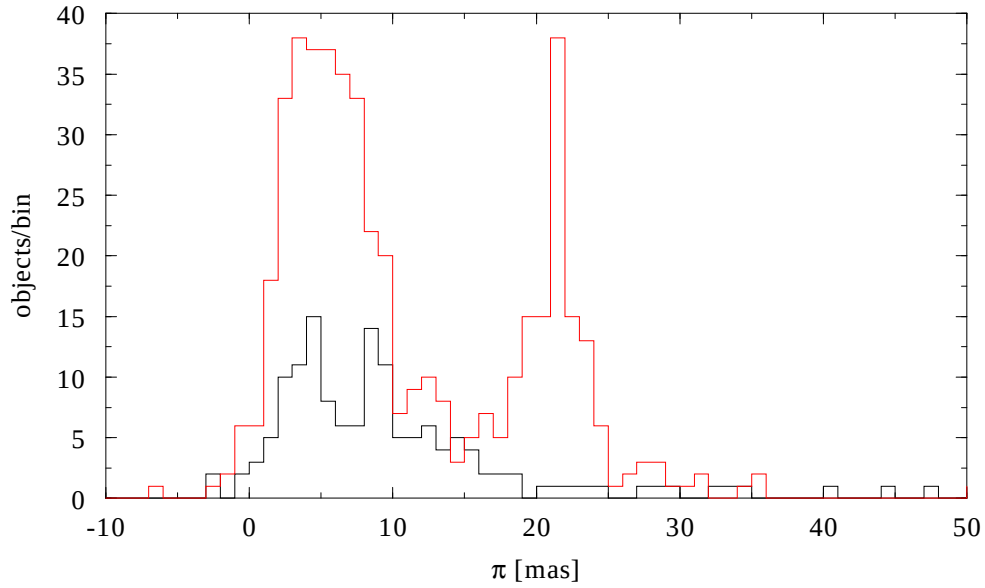

Figure 3.2.8. *Distribution of parallaxes in two selected regions of the sky (bin size 1 mas). Black line: stars with* $10° < l < 20°$, $13° < b < 23°$ *(including the Ophiuchus dark nebula). Red line: stars with* $170° < l < 195°$, $-25° < b < -18°$ *(including most Hyades cluster members).*

Figure 3.2.9. *Hipparcos Catalogue, Field H12: median proper motion in galactic longitude, in galactic coordinates (cell size $2^\circ \times 2^\circ$). The bipolar structure of the plot results from the motion of the solar system towards the apex (see text).*

Figure 3.2.10. *Hipparcos Catalogue, Field H12: median proper motion in right ascension, in equatorial coordinates (cell size $2^\circ \times 2^\circ$). The solar motion accounts for the preferentially positive proper motions at $\alpha = 0^\circ$ and negative values at $\alpha = 180^\circ$.*

Figure 3.2.11. *Hipparcos Catalogue, Field H13: median proper motion in galactic latitude, in galactic coordinates (cell size $2^\circ \times 2^\circ$).*

Figure 3.2.12. *Hipparcos Catalogue, Field H13: median proper motion in declination, in equatorial coordinates (cell size $2^\circ \times 2^\circ$).*

Figure 3.2.13. *Hipparcos Catalogue, Field H12: median component of transverse velocity in galactic longitude for stars with parallax $\pi > 7.5$ mas, in galactic coordinates (cell size $2^\circ \times 2^\circ$). The distribution has been smoothed over the eight closest neighbours of each cell. The bipolar structure of the plot results from the motion of the solar system towards the apex.*

Figure 3.2.14. *Hipparcos Catalogue, Field H13: median component of transverse velocity in galactic latitude for stars with parallax $\pi > 7.5$ mas, in galactic coordinates (cell size $2^\circ \times 2^\circ$). The distribution has been smoothed over the eight closest neighbours of each cell. The structure of the plot results from the motion of the solar system towards the apex.*

Figure 3.2.15. *Hipparcos Catalogue, Field H14: median standard error of $\alpha*$, in equatorial coordinates (cell size $2^\circ \times 2^\circ$).*

Figure 3.2.16. *Hipparcos Catalogue, Field H14: median standard error of $\lambda*$, in ecliptic coordinates (cell size $2^\circ \times 2^\circ$).*

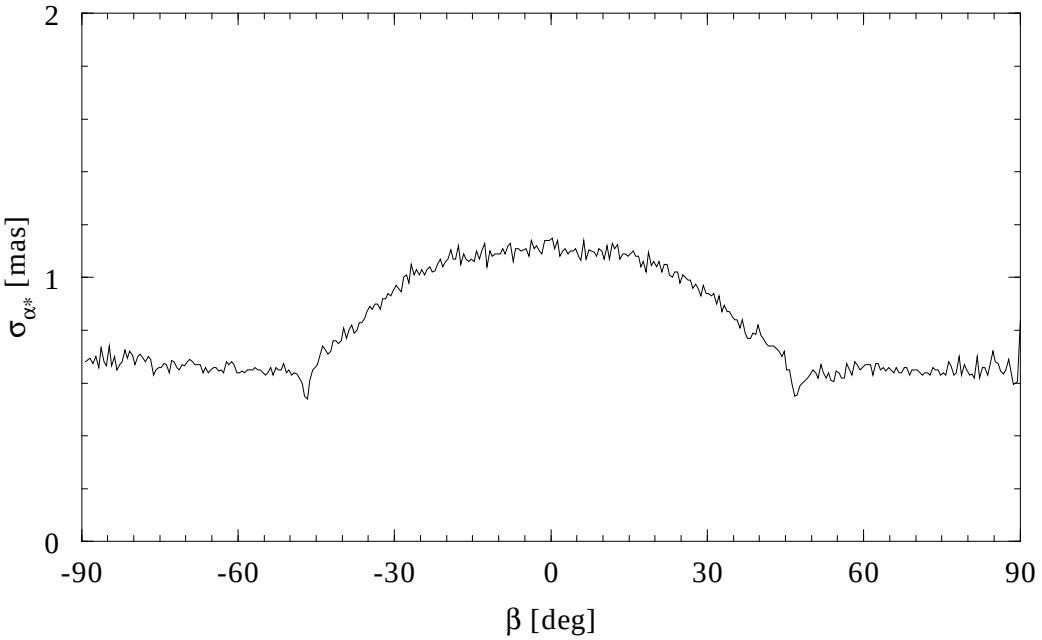

Figure 3.2.17. *Hipparcos Catalogue, Field H14: median standard error of $\alpha*$ versus ecliptic latitude (bin size 0.5°).*

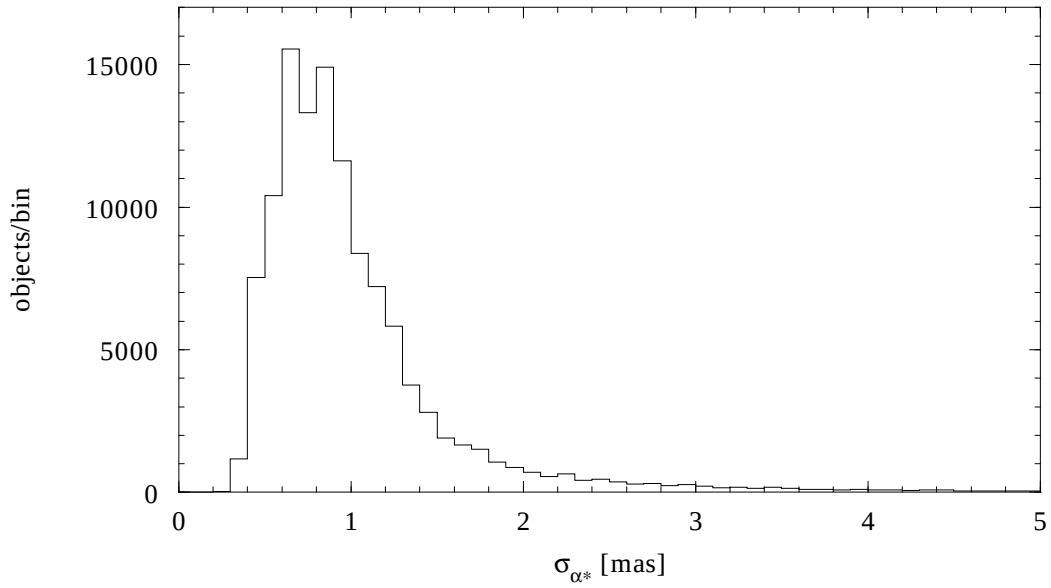

Figure 3.2.18. *Hipparcos Catalogue, Field H14: standard error of $\alpha*$ (bin size 0.1 mas).*

Figure 3.2.19. *Hipparcos Catalogue, Field H15: median standard error of δ, in equatorial coordinates (cell size $2^\circ \times 2^\circ$).*

Figure 3.2.20. *Hipparcos Catalogue, Field H15: median standard error of β, in ecliptic coordinates (cell size $2^\circ \times 2^\circ$).*

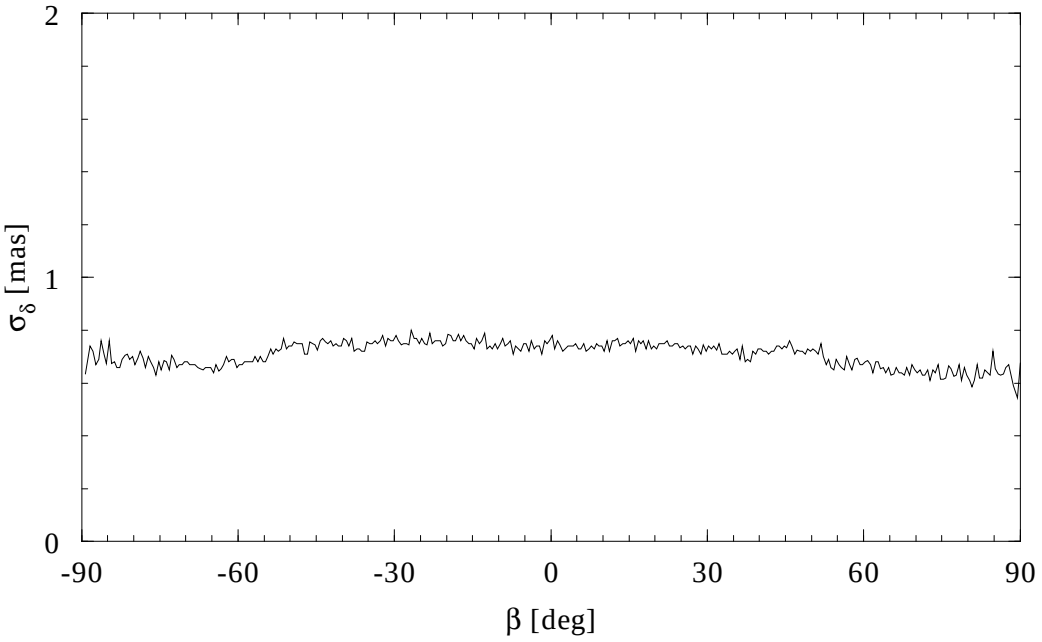

Figure 3.2.21. *Hipparcos Catalogue, Field H15: median standard error of δ versus ecliptic latitude (bin size 0.5°).*

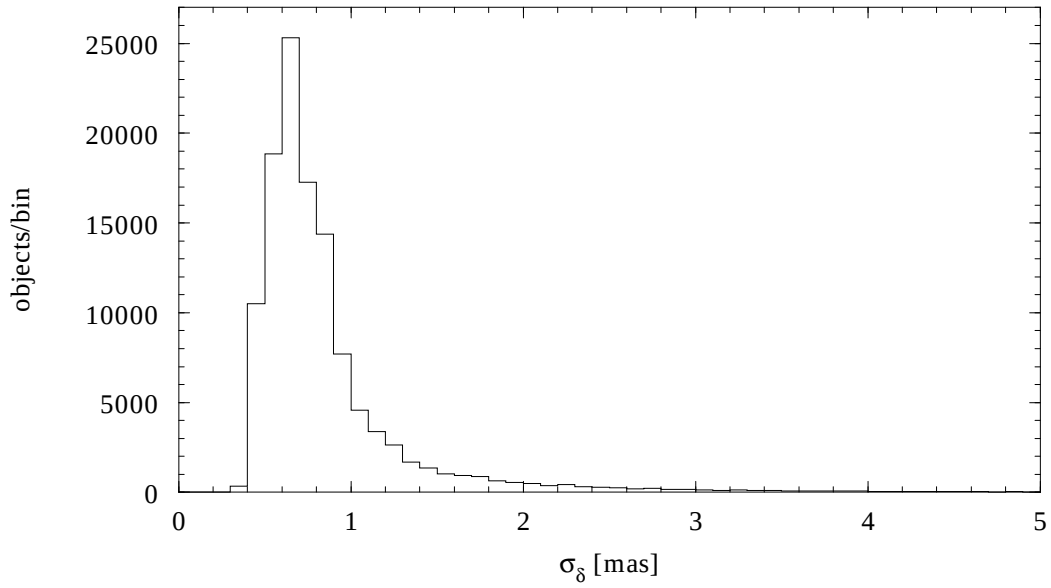

Figure 3.2.22. *Hipparcos Catalogue, Field H15: standard error of δ (bin size 0.1 mas).*

Figure 3.2.23. *Hipparcos Catalogue, Field H16: median standard error of π, in equatorial coordinates (cell size $2^\circ \times 2^\circ$).*

Figure 3.2.24. *Hipparcos Catalogue, Field H16: median standard error of π, in ecliptic coordinates (cell size $2^\circ \times 2^\circ$).*

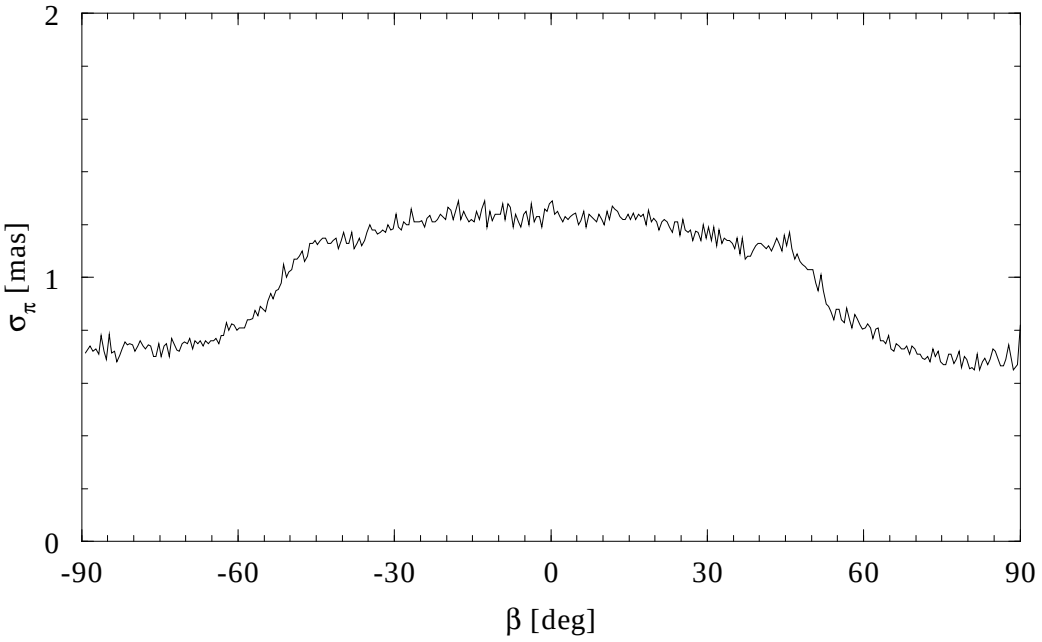

Figure 3.2.25. *Hipparcos Catalogue, Field H16: median standard error of π versus ecliptic latitude (bin size 0.5°).*

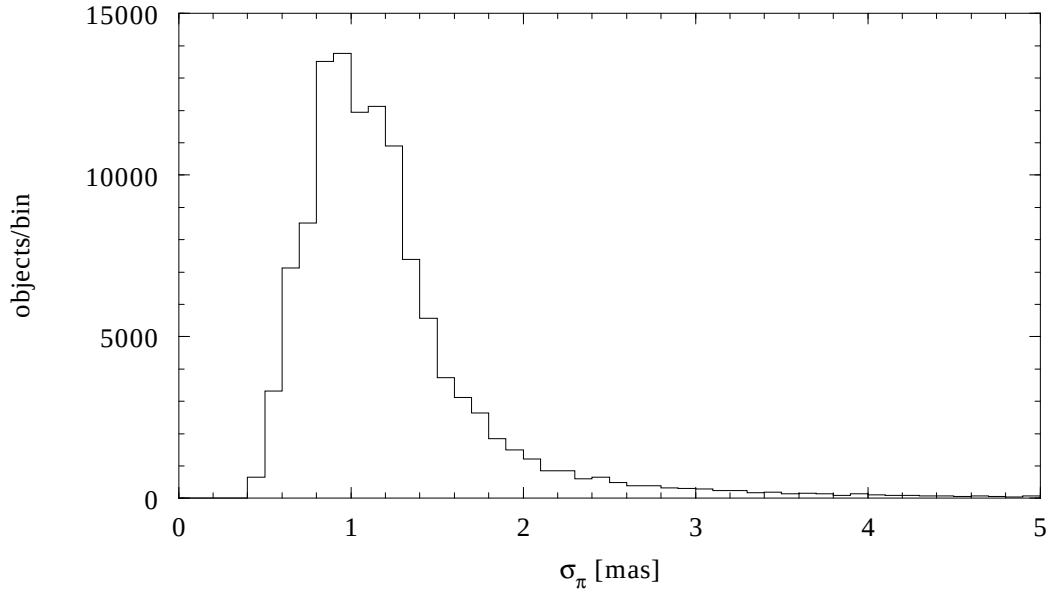

Figure 3.2.26. *Hipparcos Catalogue, Field H16: standard error of π (bin size 0.1 mas).*

Figure 3.2.27. *Hipparcos Catalogue, Field H11/H16: median relative precision of distance σ_π/π for stars with a parallax $\pi > 2$ mas, in ecliptic coordinates (cell size $2^\circ \times 2^\circ$).*

Figure 3.2.28. *Hipparcos Catalogue, Field H11/H16: median relative precision of distance σ_π/π for stars with a parallax $\pi > 7.5$ mas, in galactic coordinates (cell size $2^\circ \times 2^\circ$).*

Figure 3.2.29. *Hipparcos Catalogue, Field H17: median standard error of $\mu_{\alpha *}$, in equatorial coordinates (cell size $2^\circ \times 2^\circ$).*

Figure 3.2.30. *Hipparcos Catalogue, Field H17: median standard error of $\mu_{\lambda *}$, in ecliptic coordinates (cell size $2^\circ \times 2^\circ$).*

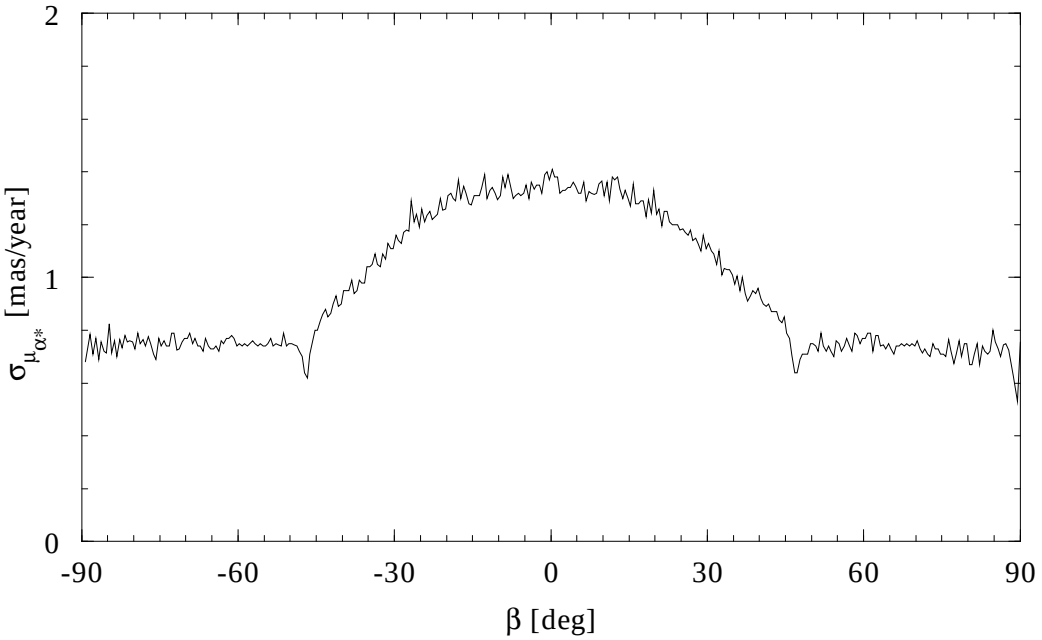

Figure 3.2.31. *Hipparcos Catalogue, Field H17: median standard error of $\mu_{\alpha*}$ versus ecliptic latitude (bin size 0.5°).*

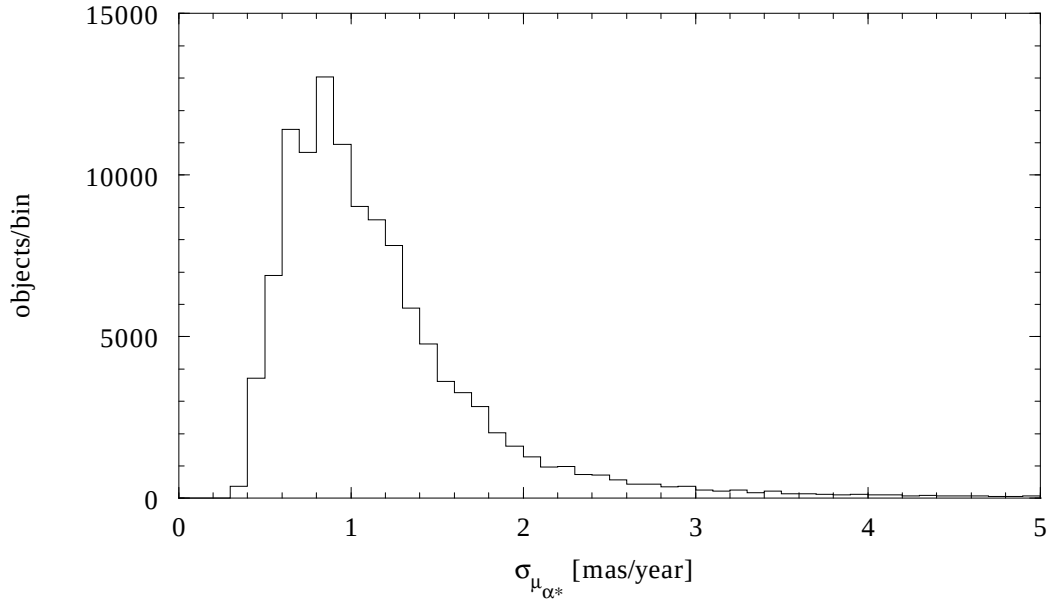

Figure 3.2.32. *Hipparcos Catalogue, Field H17: standard error of $\mu_{\alpha*}$ (bin size 0.1 mas/year).*

Figure 3.2.33. *Hipparcos Catalogue, Field H18: median standard error of μ_δ, in equatorial coordinates (cell size $2^\circ \times 2^\circ$).*

Figure 3.2.34. *Hipparcos Catalogue, Field H18: median standard error of μ_β, in ecliptic coordinates (cell size $2^\circ \times 2^\circ$). The distribution is almost independent of the latitude for the same reasons as for the standard error of the ecliptic latitude. The remaining effect in longitude is due to the time distribution of the observations.*

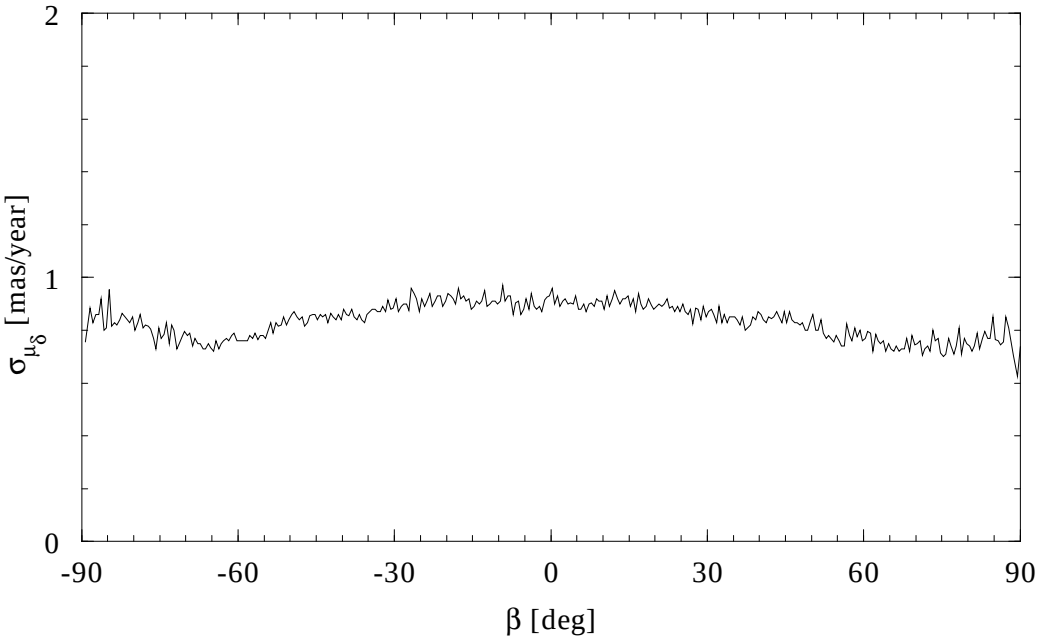

Figure 3.2.35. *Hipparcos Catalogue, Field H18: median standard error of μ_δ versus ecliptic latitude (bin size 0.5°).*

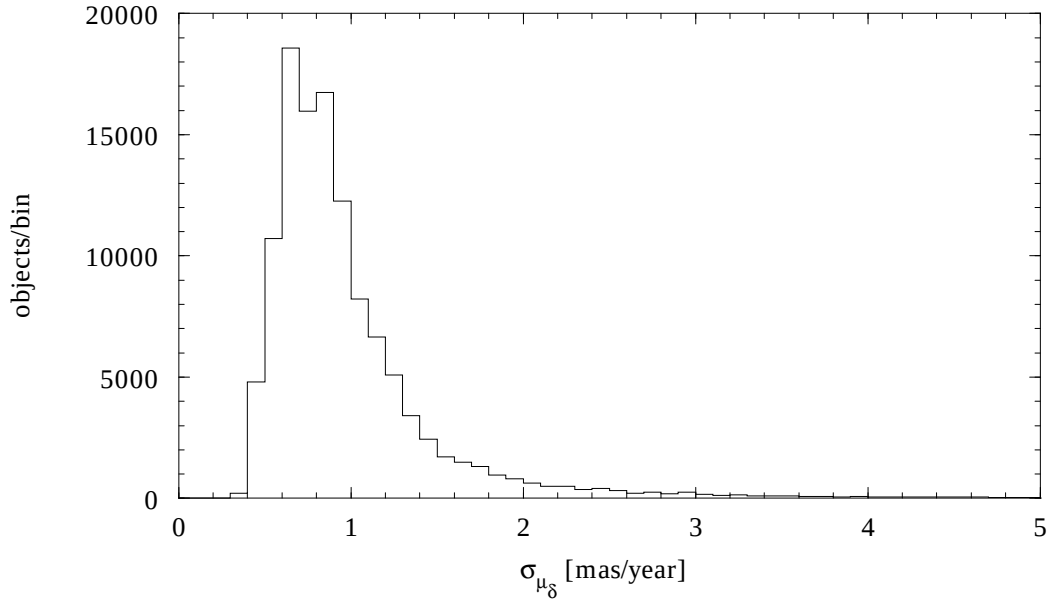

Figure 3.2.36. *Hipparcos Catalogue, Field H18: standard error of μ_δ (bin size 0.1 mas/year).*

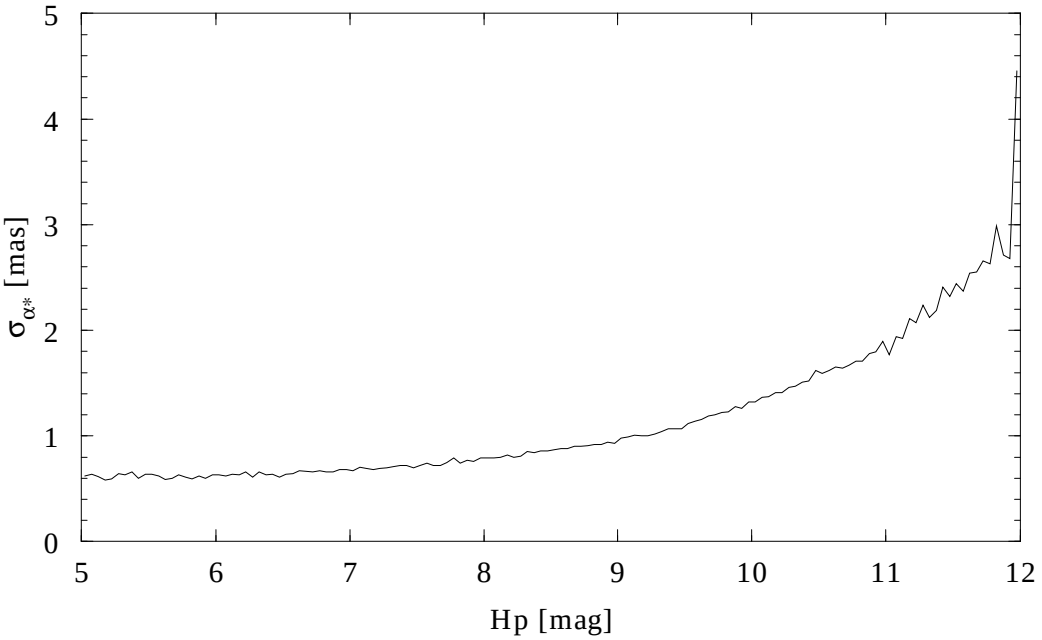

Figure 3.2.37. *Hipparcos Catalogue, Field H14: median standard error of $\alpha*$ versus Hp (bin size 0.05 mag).*

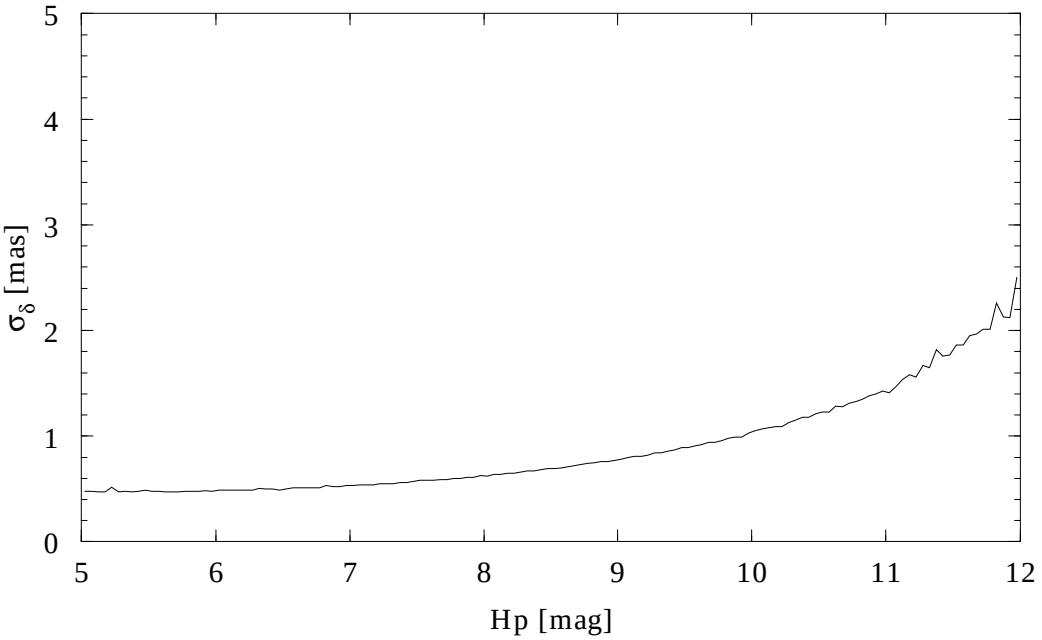

Figure 3.2.38. *Hipparcos Catalogue, Field H15: median standard error of δ versus Hp (bin size 0.05 mag).*

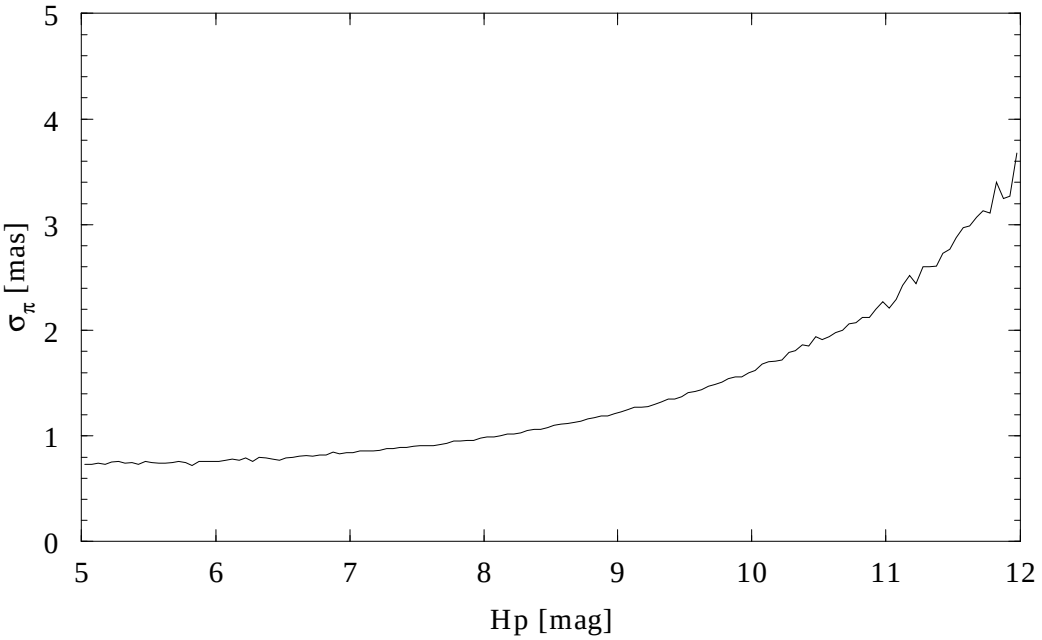

Figure 3.2.39. *Hipparcos Catalogue, Field H16: median standard error of π versus Hp (bin size 0.05 mag).*

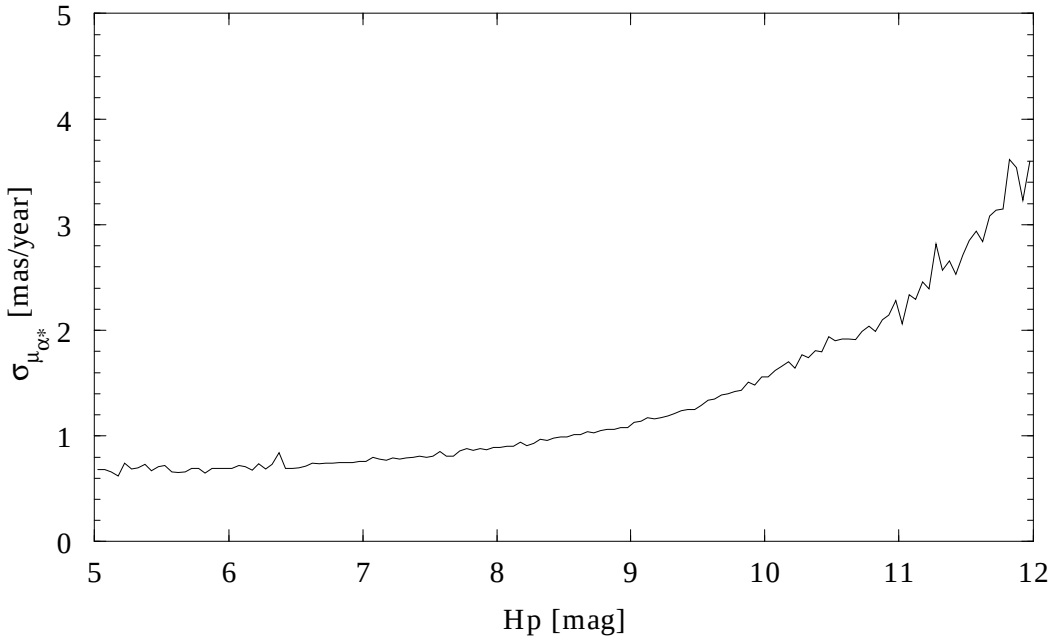

Figure 3.2.40. *Hipparcos Catalogue, Field H17: median standard error of $\mu_{\alpha*}$ versus Hp (bin size 0.05 mag).*

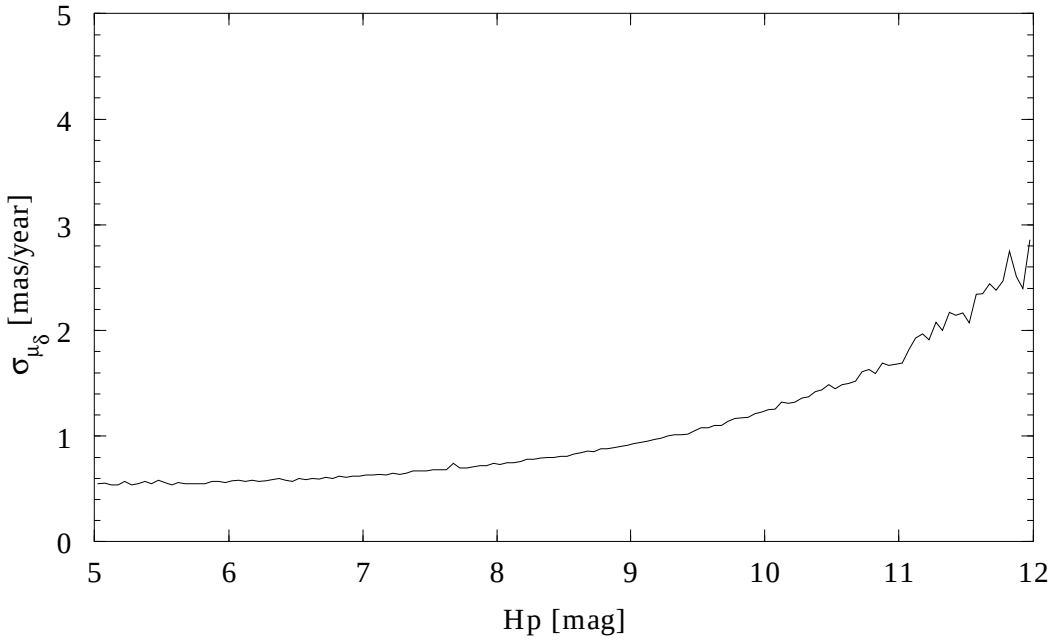

Figure 3.2.41. *Hipparcos Catalogue, Field H18: median standard error of μ_δ versus Hp (bin size 0.05 mag).*

Figure 3.2.42. *Hipparcos Catalogue, Field H19: median correlation between $\alpha*$ and δ in equatorial coordinates (cell size $2^\circ \times 2^\circ$). The systematic strucure is caused by the transformation from ecliptic to equatorial coordinates, see text.*

Figure 3.2.43. *Hipparcos Catalogue, Field H19: median correlation between $\lambda*$ and β in ecliptic coordinates (cell size $2^\circ \times 2^\circ$). Features are clearly connected to the scanning law.*

Figure 3.2.44. *Hipparcos Catalogue, Field H20: median correlation between $\alpha*$ and π in equatorial coordinates (cell size $2^\circ \times 2^\circ$).*

Figure 3.2.45. *Hipparcos Catalogue, Field H20: median correlation between $\lambda*$ and π in ecliptic coordinates (cell size $2^\circ \times 2^\circ$). The variations are very large over the sky with much structure. The strong asymmetry with the ecliptic longitude is due to a lack of symmetry in the distribution of the observations with respect to the position of the sun (see text).*

Figure 3.2.46. *Hipparcos Catalogue, Field H21: median correlation between δ and π in equatorial coordinates (cell size $2^\circ \times 2^\circ$).*

Figure 3.2.47. *Hipparcos Catalogue, Field H21: median correlation between β and π in ecliptic coordinates (cell size $2^\circ \times 2^\circ$). The variations are not prominent over the sky and show little structure. The bias towards negative values is explained in the text.*

Figure 3.2.48. *Hipparcos Catalogue, Field H22: median correlation between $\alpha*$ and $\mu_{\alpha*}$ in equatorial coordinates (cell size $2^\circ \times 2^\circ$).*

Figure 3.2.49. *Hipparcos Catalogue, Field H22: median correlation between $\lambda*$ and $\mu_{\lambda*}$ in ecliptic coordinates (cell size $2^\circ \times 2^\circ$). This correlation coefficient should be zero whenever the observations are distributed symmetrically with respect to the Catalogue epoch. The plot reflects the distribution of the mean epoch of each star (cf. Figure 3.2.62) combined with the latitude effect in the standard error of the longitude.*

Figure 3.2.50. *Hipparcos Catalogue, Field H23: median correlation between δ and $\mu_{\alpha*}$ in equatorial coordinates (cell size $2^\circ \times 2^\circ$).*

Figure 3.2.51. *Hipparcos Catalogue, Field H23: median correlation between β and $\mu_{\lambda*}$ in ecliptic coordinates (cell size $2^\circ \times 2^\circ$). All the features in this plot are linked to the scanning law.*

Figure 3.2.52. *Hipparcos Catalogue, Field H24: median correlation between π and $\mu_{\alpha*}$ in equatorial coordinates (cell size $2^\circ \times 2^\circ$).*

Figure 3.2.53. *Hipparcos Catalogue, Field H24: median correlation between π and $\mu_{\lambda*}$ in ecliptic coordinates (cell size $2^\circ \times 2^\circ$). The global bipolar structure has the same cause as the strong effect observed in the correlation between the parallax and the ecliptic longitude.*

Figure 3.2.54. *Hipparcos Catalogue, Field H25: median correlation between $\alpha*$ and μ_δ in equatorial coordinates (cell size $2^\circ \times 2^\circ$).*

Figure 3.2.55. *Hipparcos Catalogue, Field H25: median correlation between $\lambda*$ and μ_β in ecliptic coordinates (cell size $2^\circ \times 2^\circ$). The thread-like features are linked to the scanning law.*

Figure 3.2.56. *Hipparcos Catalogue, Field H26: median correlation between δ and μ_δ in equatorial coordinates (cell size $2^\circ \times 2^\circ$).*

Figure 3.2.57. *Hipparcos Catalogue, Field H26: median correlation between β and μ_β in ecliptic coordinates (cell size $2^\circ \times 2^\circ$). This correlation coefficient should be zero whenever the observations are distributed symmetrically with respect to the Catalogue epoch. The plot reflects the distribution of the mean epoch of each star (cf. Figure 3.2.62) combined with the (very small) latitude effect in the standard error of the longitude. The observations performed in the sun-pointing mode show up as a narrow strip close to $\lambda = 0^\circ$ and $\lambda = 180^\circ$.*

Figure 3.2.58. *Hipparcos Catalogue, Field H27: median correlation between π and μ_δ in equatorial coordinates (cell size $2^\circ \times 2^\circ$).*

Figure 3.2.59. *Hipparcos Catalogue, Field H27: median correlation between π and μ_β in ecliptic coordinates (cell size $2^\circ \times 2^\circ$). The features are connected to the time distribution of the observations.*

Figure 3.2.60. *Hipparcos Catalogue, Field H28: median correlation between $\mu_{\alpha*}$ and μ_δ in equatorial coordinates (cell size $2^\circ \times 2^\circ$). The variations over the sky are due to the transformation from ecliptic to equatorial coordinates, see text.*

Figure 3.2.61. *Hipparcos Catalogue, Field H28: median correlation between $\mu_{\lambda*}$ and μ_β in ecliptic coordinates (cell size $2^\circ \times 2^\circ$). The features are related to the time distribution of the observations, with a global variation over the sky.*

Figure 3.2.62. *Hipparcos Catalogue: median of the mean observation epoch relative to J1991.25, in ecliptic coordinates (cell size $2^\circ \times 2^\circ$). The loop structure in the range of latitude $\pm 47^\circ$ is a consequence of the scanning law and of the limited duration of the mission. The meridian strip at the centre of the plot corresponds to the region of the sky observed during the sun-pointing period at the end of the mission. The rest of this circle is visible at $\lambda \sim -170^\circ$.*

Figure 3.2.63. *Hipparcos Catalogue: median effective observation epoch relative to J1991.25, as defined in Equation 1.2.10, in ecliptic coordinates (cell size $2^\circ \times 2^\circ$).*

Figure 3.2.64. *Hipparcos Catalogue: median duration between first and last observation, in ecliptic coordinates (cell size $2^\circ \times 2^\circ$). The features are a direct consequence of the scanning law, the mission duration, and the observation interruptions.*

Figure 3.2.65. *Hipparcos Catalogue: median difference between mean observational epoch in right ascension and in declination, in ecliptic coordinates (cell size $2^\circ \times 2^\circ$).*

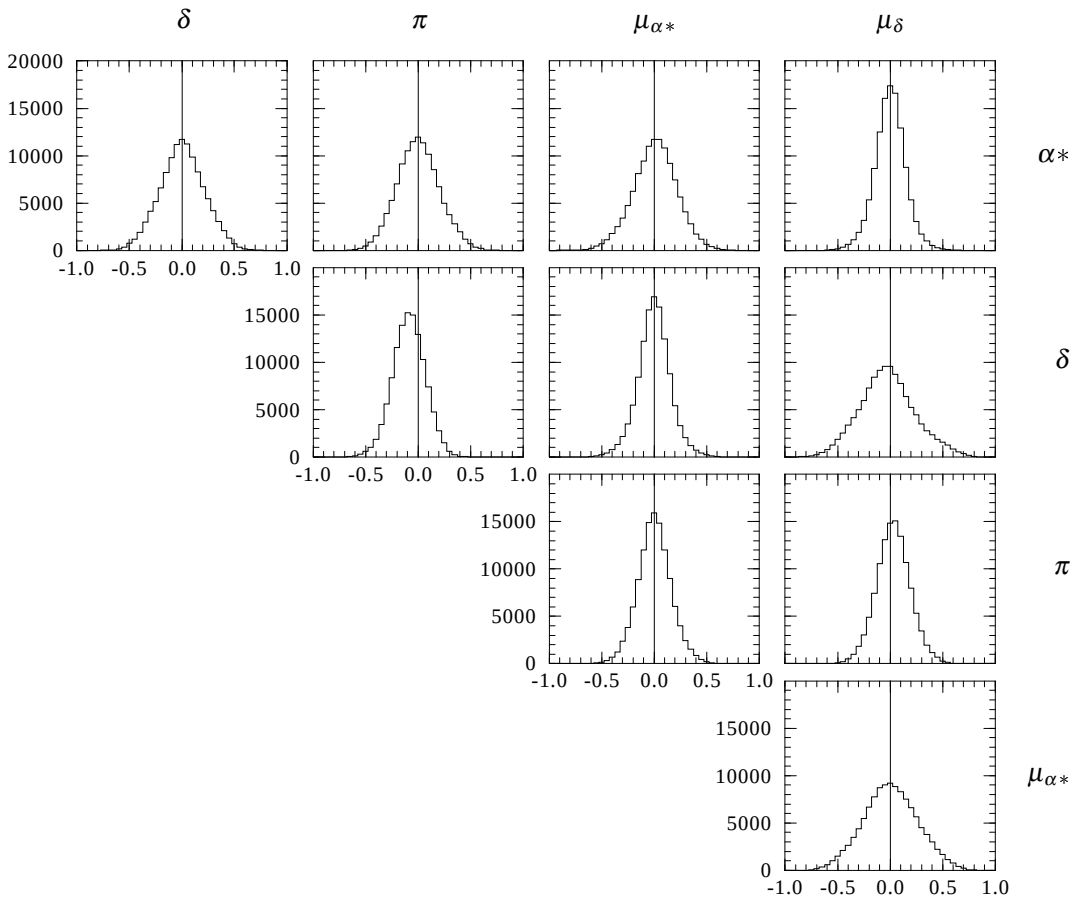

Figure 3.2.66. *Hipparcos Catalogue, Field H19–H28: correlations between astrometric parameters (bin size 0.05). The main features of these correlations, in particular the asymmetry in the π versus δ correlation, are described in the text.*

Figure 3.2.67. *Hipparcos Catalogue, Field H29: median percentage of rejected observations, F1, in ecliptic coordinates (cell size $2^\circ \times 2^\circ$).*

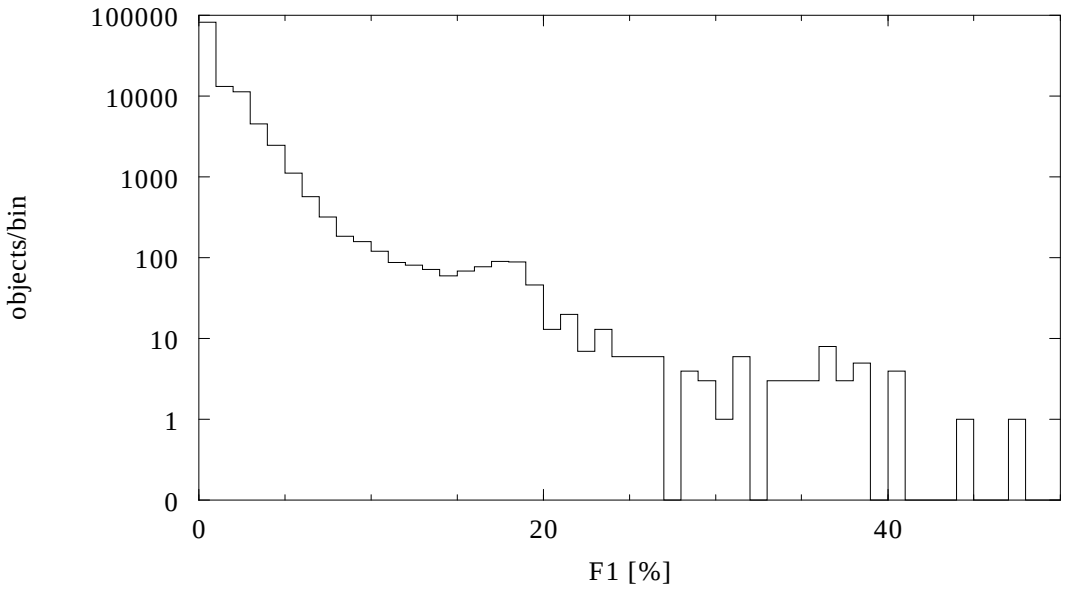

Figure 3.2.68. *Hipparcos Catalogue, Field H29: percentage of rejected observations, F1 (bin size 1%).*

Figure 3.2.69. *Hipparcos Catalogue, Field H30: median goodness-of-fit, F2, in ecliptic coordinates (cell size $2^\circ \times 2^\circ$). The structure indicates that the adjustment is slightly less satisfactory around the ecliptic than around the ecliptic poles.*

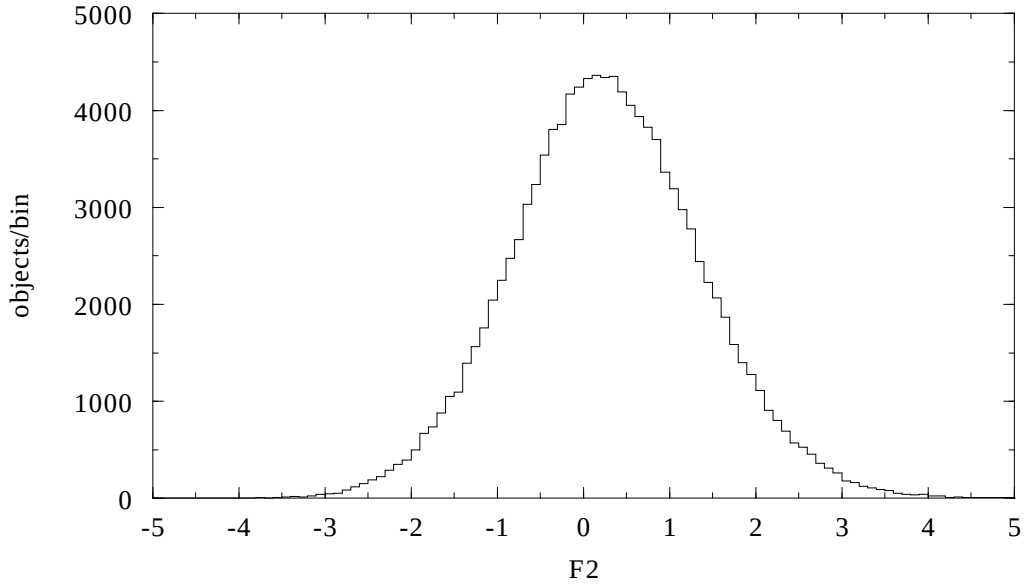

Figure 3.2.70. *Hipparcos Catalogue, Field H30: goodness-of-fit, F2 (bin size 0.1).*

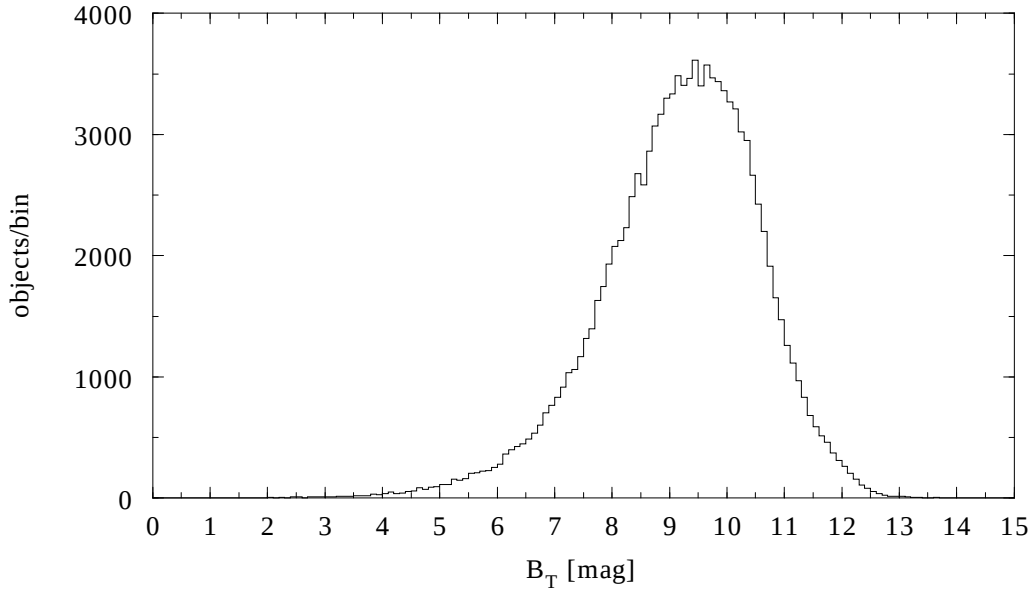

Figure 3.2.71. *Hipparcos Catalogue, Field H32: B_T magnitude (bin size 0.1 mag).*

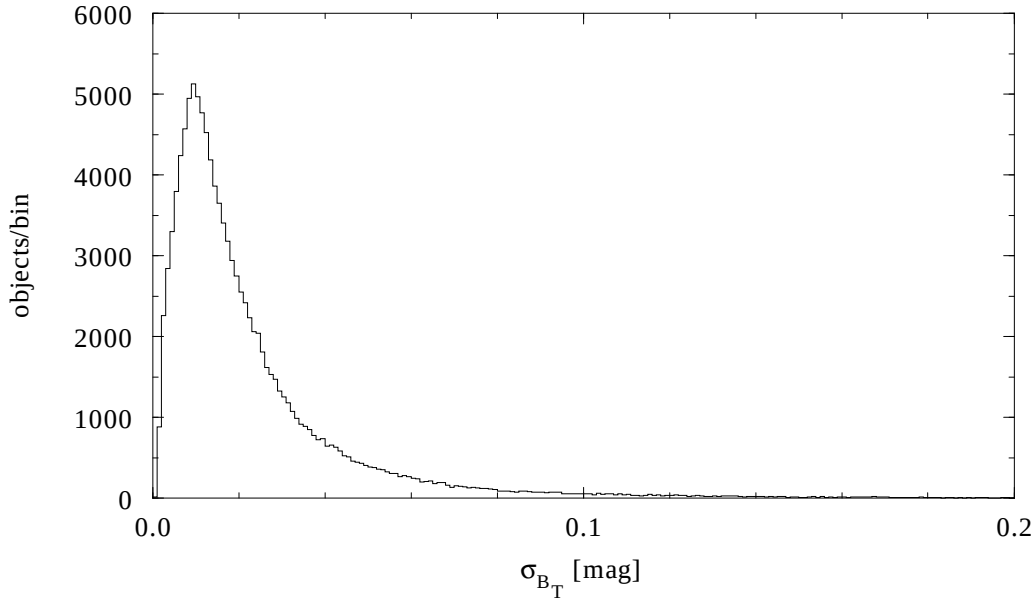

Figure 3.2.72. *Hipparcos Catalogue, Field H33: standard error in B_T magnitude (bin size 0.001 mag).*

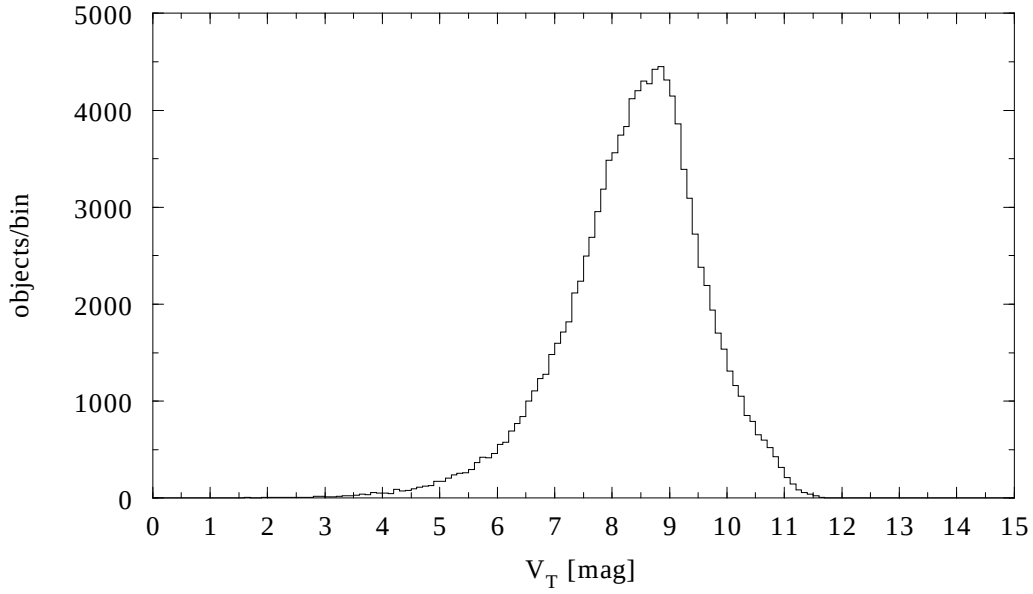

Figure 3.2.73. *Hipparcos Catalogue, Field H34: V_T magnitude (bin size 0.1 mag).*

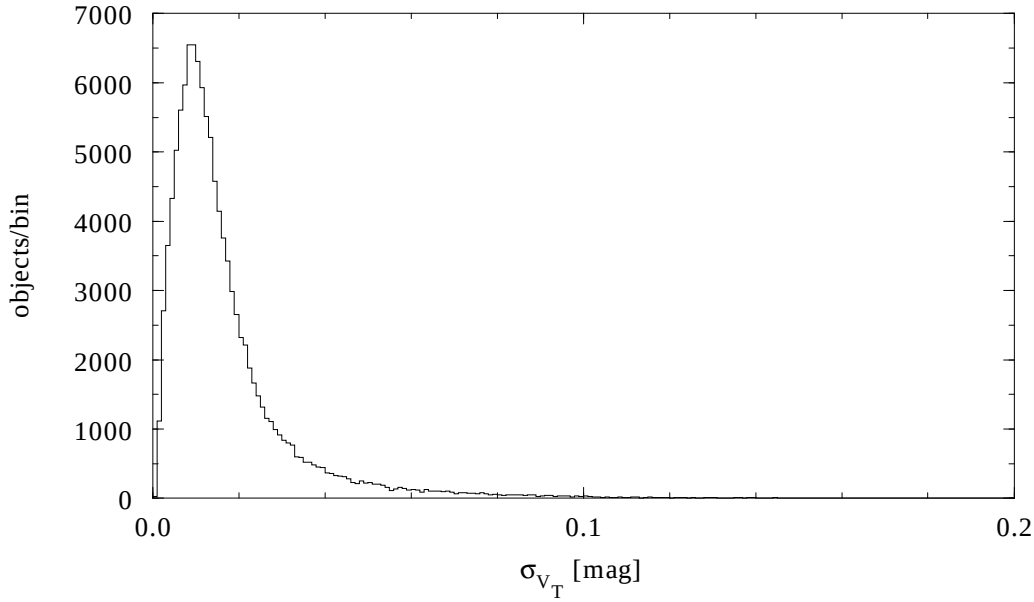

Figure 3.2.74. *Hipparcos Catalogue, Field H35: standard error in V_T magnitude (bin size 0.001 mag).*

Figure 3.2.75. *Hipparcos Catalogue, Field H37: median colour index $B-V$, in galactic coordinates (cell size $2^\circ \times 2^\circ$). As expected most of the early-type stars are in the galactic plane while on the average those outside this plane are redder.*

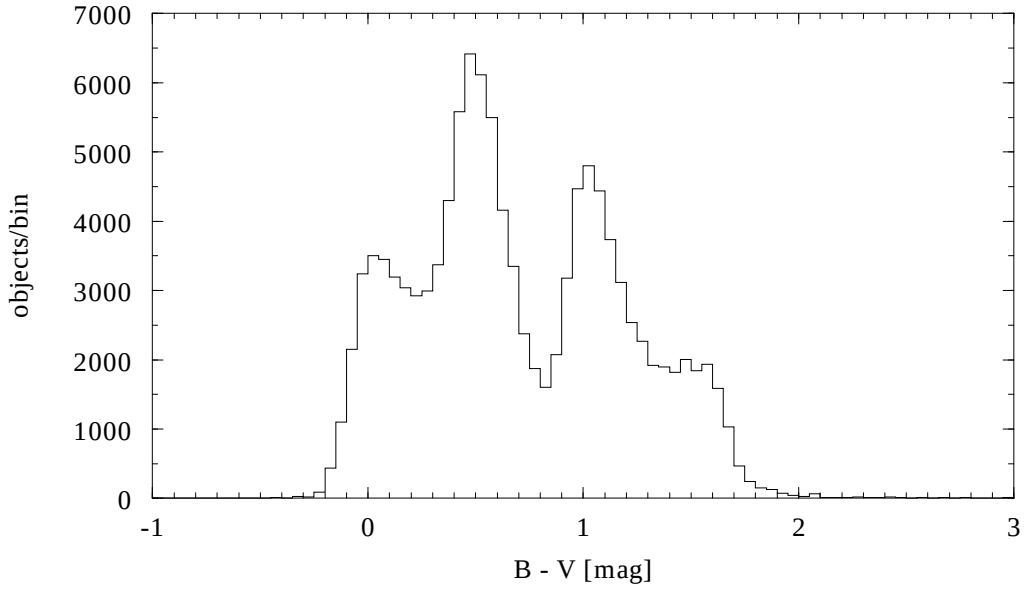

Figure 3.2.76. *Hipparcos Catalogue, Field H37: colour index $B-V$ (bin size 0.05 mag).*

Figure 3.2.77. *Hipparcos Catalogue, Field H40: median colour index $V - I$, in galactic coordinates (cell size $2^\circ \times 2^\circ$). Most of the early-type stars are in the galactic plane while on the average those outside this plane are redder.*

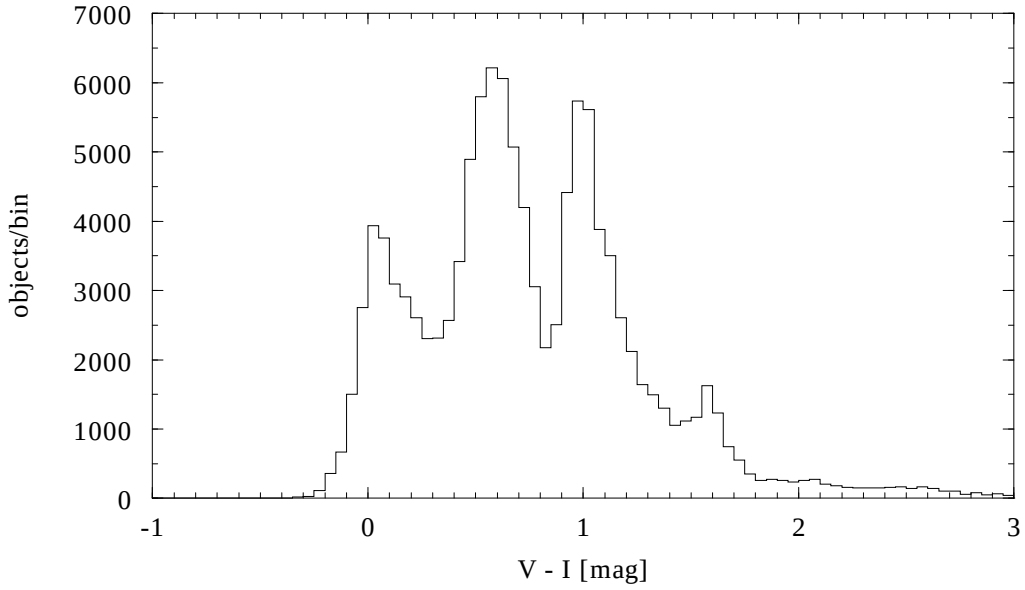

Figure 3.2.78. *Hipparcos Catalogue, Field H40: colour index $V - I$ (bin size 0.05 mag).*

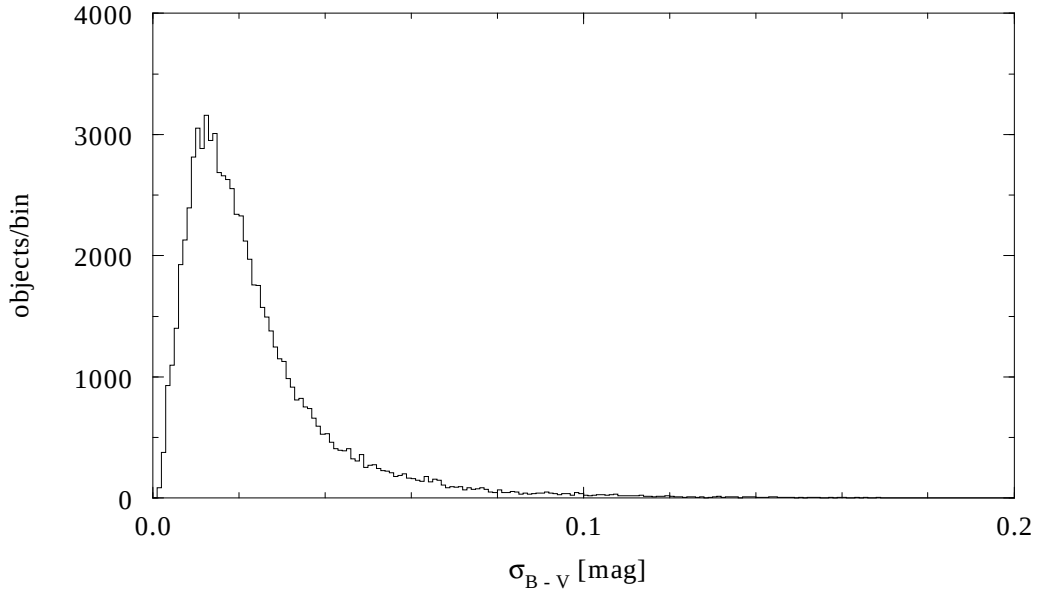

Figure 3.2.79. *Hipparcos Catalogue, Field H38: standard error in colour index $B - V$ for objects with Field H39 = 'T' (bin size 0.001 mag).*

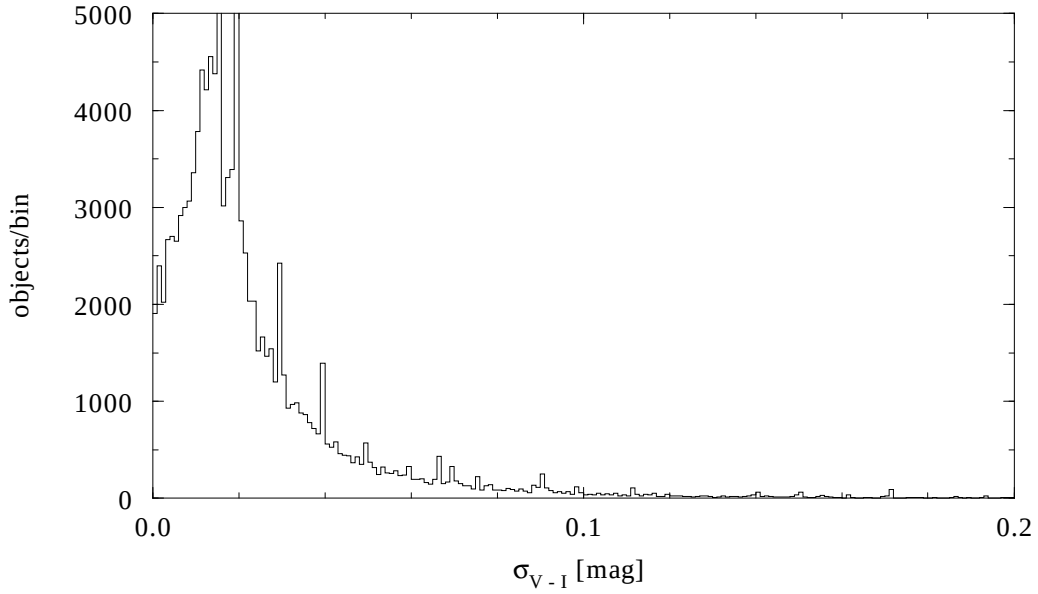

Figure 3.2.80. *Hipparcos Catalogue, Field H41: standard error in colour index $V - I$ (bin size 0.001 mag).*

Figure 3.2.81. *Hipparcos Catalogue, Field H44: median Hp magnitude, in galactic coordinates (cell size $2^\circ \times 2^\circ$). The average of the Catalogue is Hp ~ 8.5 mag with significant variations with galactic latitude.*

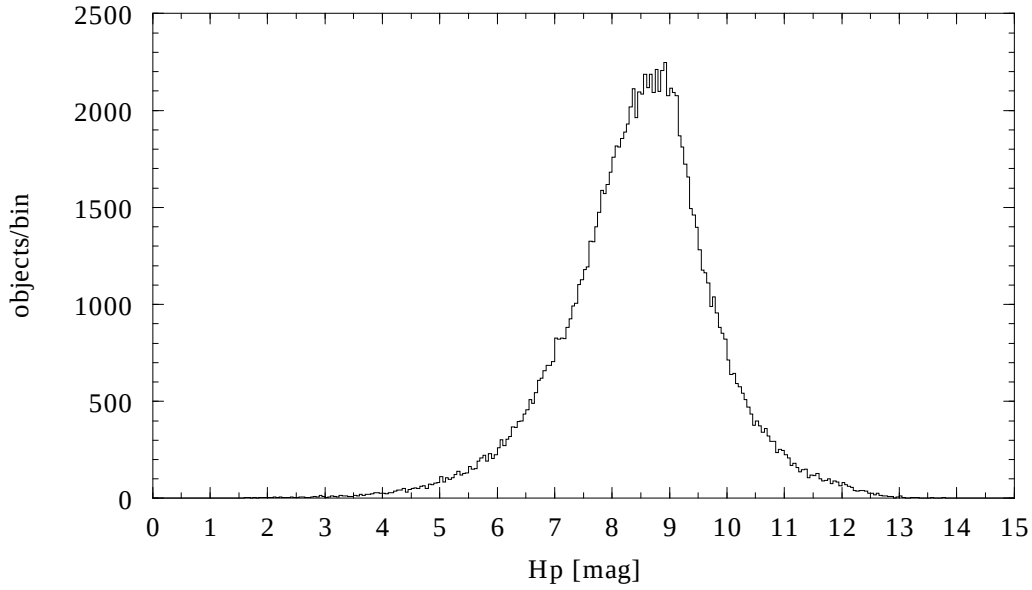

Figure 3.2.82. *Hipparcos Catalogue, Field H44: median Hp magnitude (bin size 0.05 mag).*

Figure 3.2.83. *Hipparcos Catalogue, Field H45: median standard error in Hp magnitude, in galactic coordinates (cell size $2° \times 2°$). The main structure is connected to the magnitude distribution.*

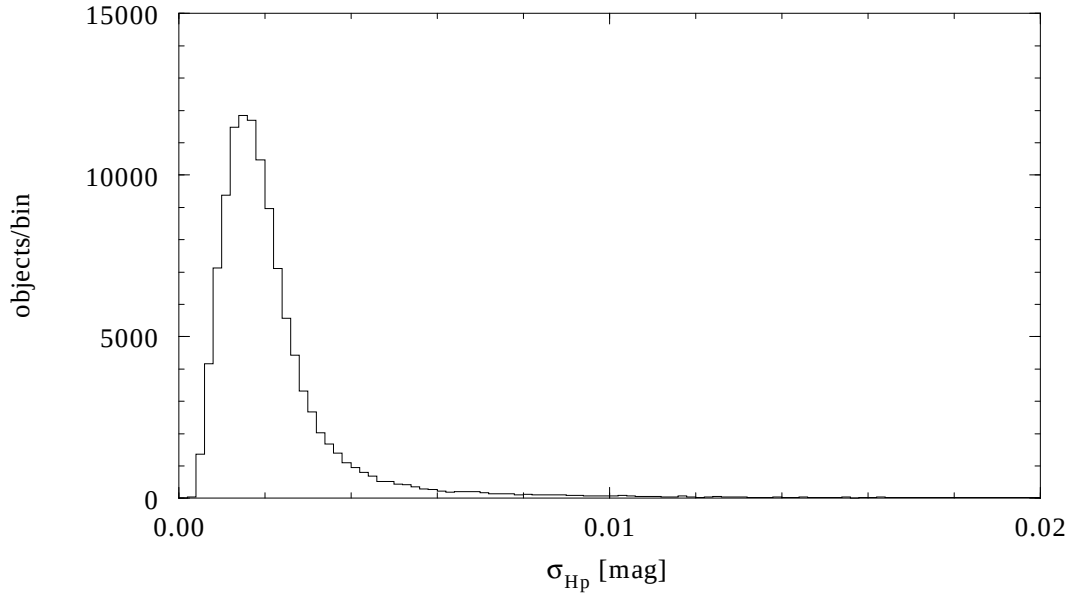

Figure 3.2.84. *Hipparcos Catalogue, Field H45: standard error in Hp magnitude (bin size 0.0002 mag).*

Figure 3.2.85. *Hipparcos Catalogue, Field H46: median scatter in Hp magnitude, in ecliptic coordinates (cell size $2^\circ \times 2^\circ$).*

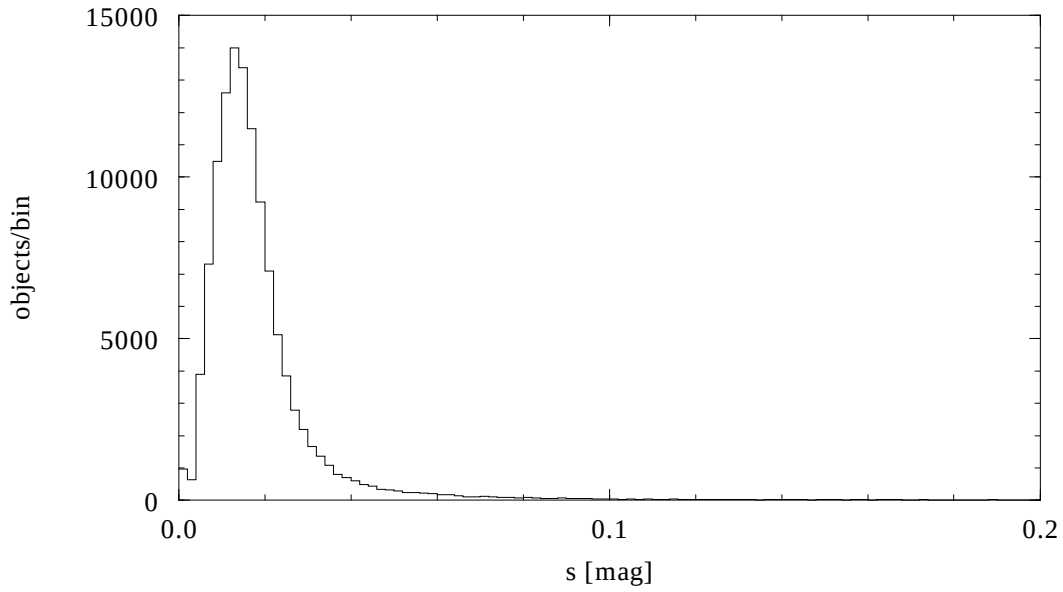

Figure 3.2.86. *Hipparcos Catalogue, Field H46: scatter in Hp magnitude (bin size 0.002 mag).*

Figure 3.2.87. *Hipparcos Catalogue, Field H47: median number of accepted photometric transits, in ecliptic coordinates (cell size $2^\circ \times 2^\circ$). The structure reflects the properties of the scanning law and the limited duration of the mission.*

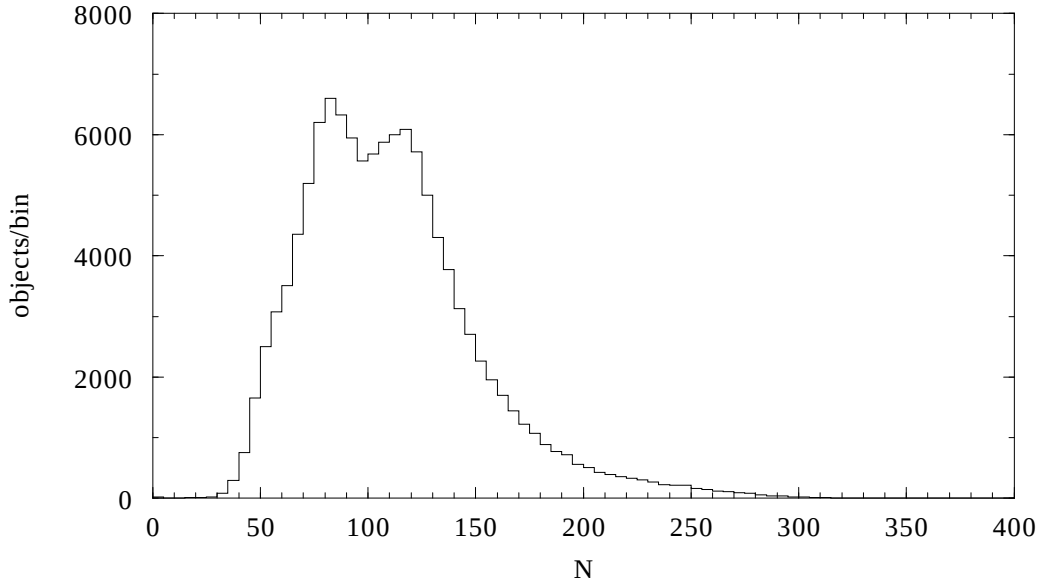

Figure 3.2.88. *Hipparcos Catalogue, Field H47: number of accepted photometric transits, N (bin size 5).*

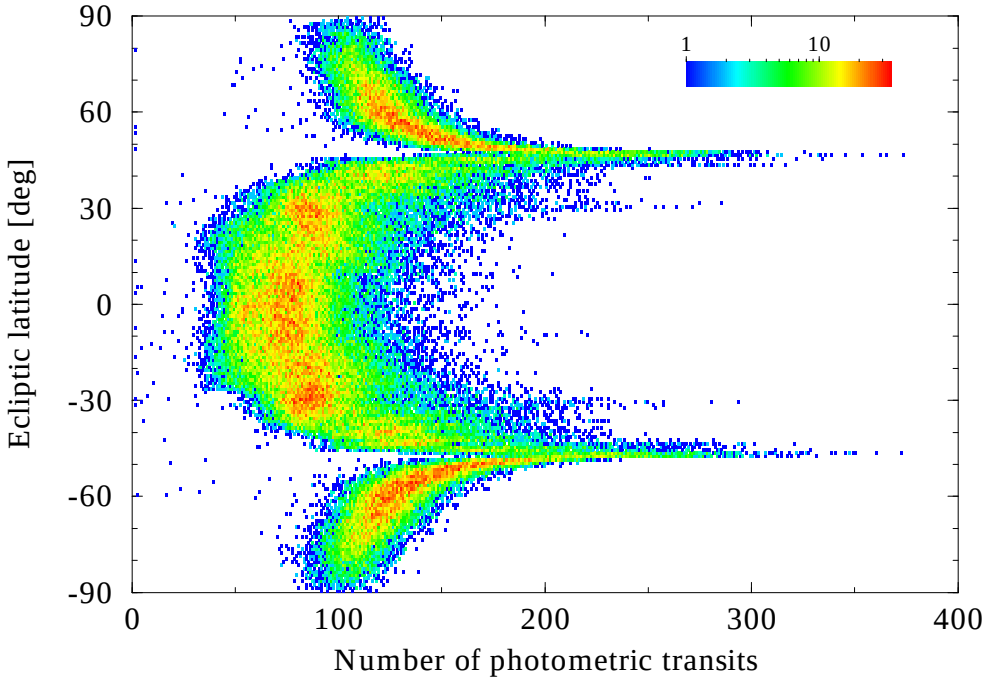

Figure 3.2.89. *Hipparcos Catalogue, Field H47: number of accepted photometric transits versus ecliptic latitude, as a density plot. Scale indicates number of stars per bin of 1 transit $\times 1^\circ$.*

Available on disk 6

Figure 3.2.90. *Hipparcos Catalogue, Fields H49/H50: median difference between the observed magnitude Hp at minimum and maximum luminosities, in ecliptic coordinates (cell size $2^\circ \times 2^\circ$). The pattern is similar to that seen in the sky distribution of the scatter.*

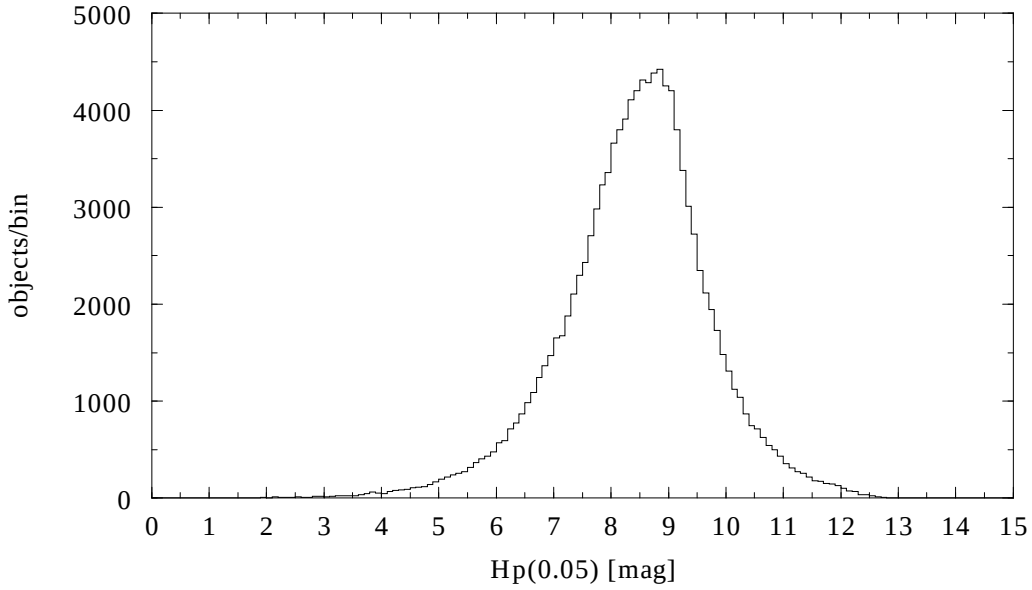

Figure 3.2.91. *Hipparcos Catalogue, Field H49: Hp magnitude, 5th percentile (bin size 0.1 mag).*

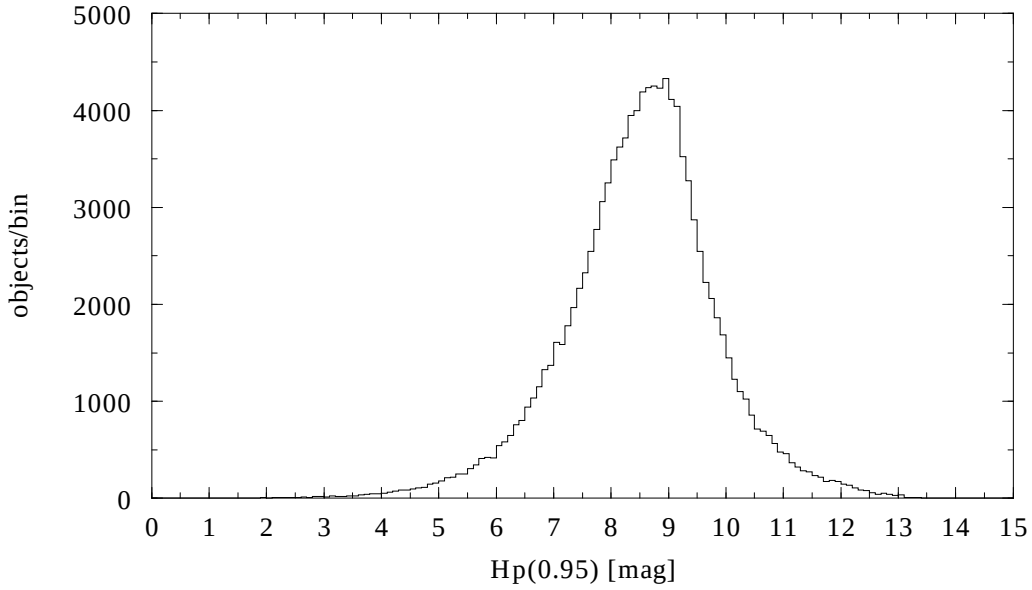

Figure 3.2.92. *Hipparcos Catalogue, Field H50: Hp magnitude, 95th percentile (bin size 0.1 mag).*

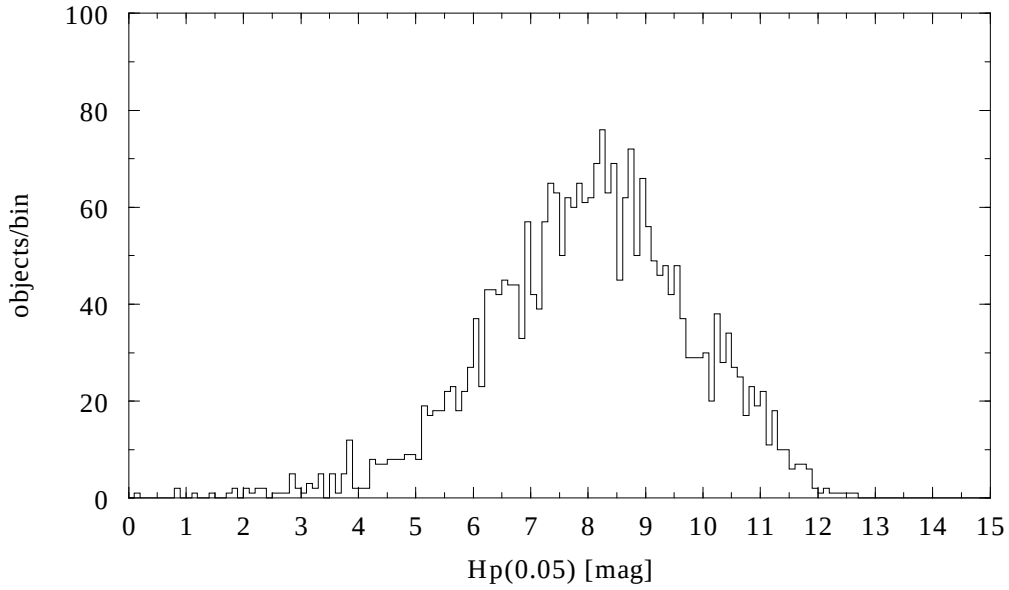

Figure 3.2.93. *Hipparcos Catalogue, Field H49: Hp magnitude, 5th percentile for objects in Section 1 of the Variability Annex (Periodic Variables) (bin size 0.1 mag).*

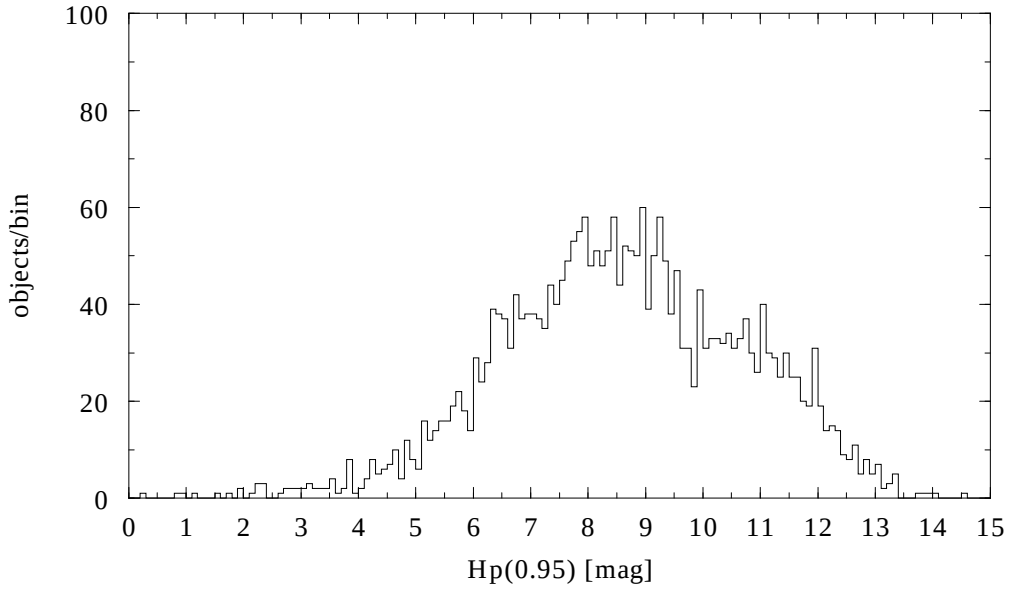

Figure 3.2.94. *Hipparcos Catalogue, Field H50: Hp magnitude, 95th percentile for objects in Section 1 of the Variability Annex (Periodic Variables) (bin size 0.1 mag).*

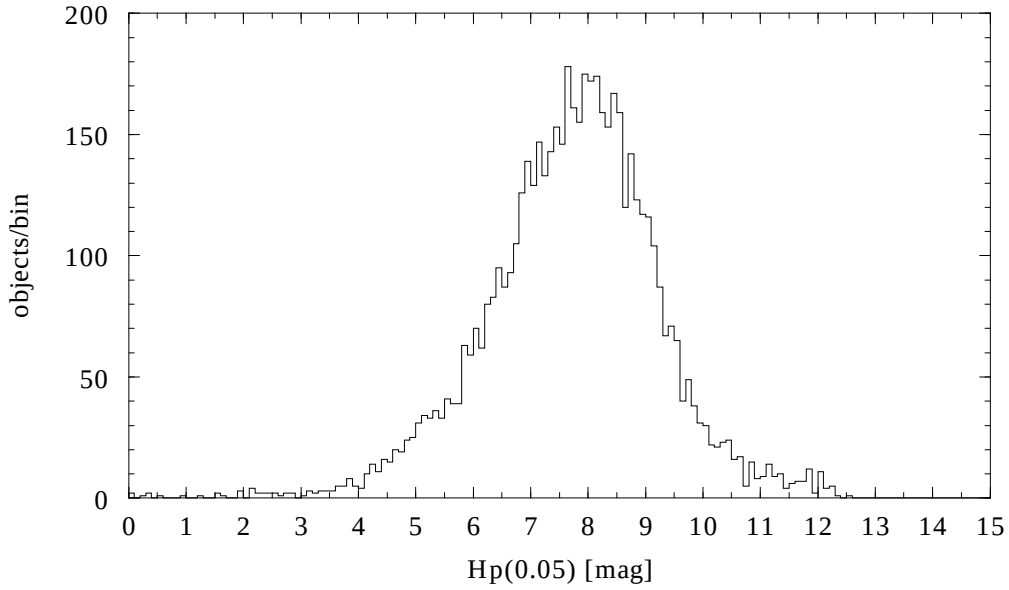

Figure 3.2.95. *Hipparcos Catalogue, Field H49: Hp magnitude, 5th percentile for objects in Section 2 of the Variability Annex (Unsolved Variables) (bin size 0.1 mag).*

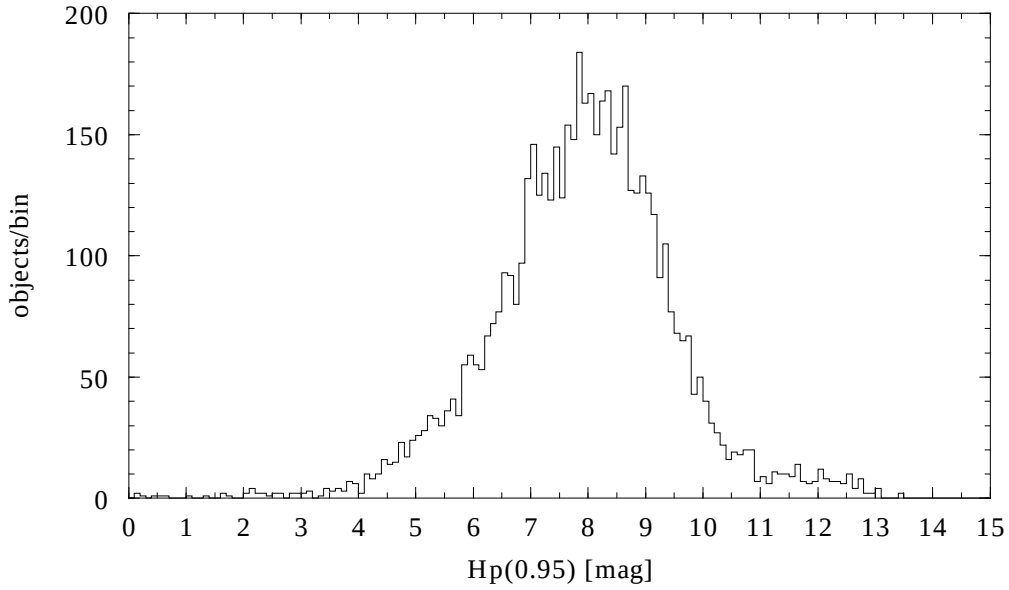

Figure 3.2.96. *Hipparcos Catalogue, Field H50: Hp magnitude, 95th percentile for objects in Section 2 of the Variability Annex (Unsolved Variables) (bin size 0.1 mag).*

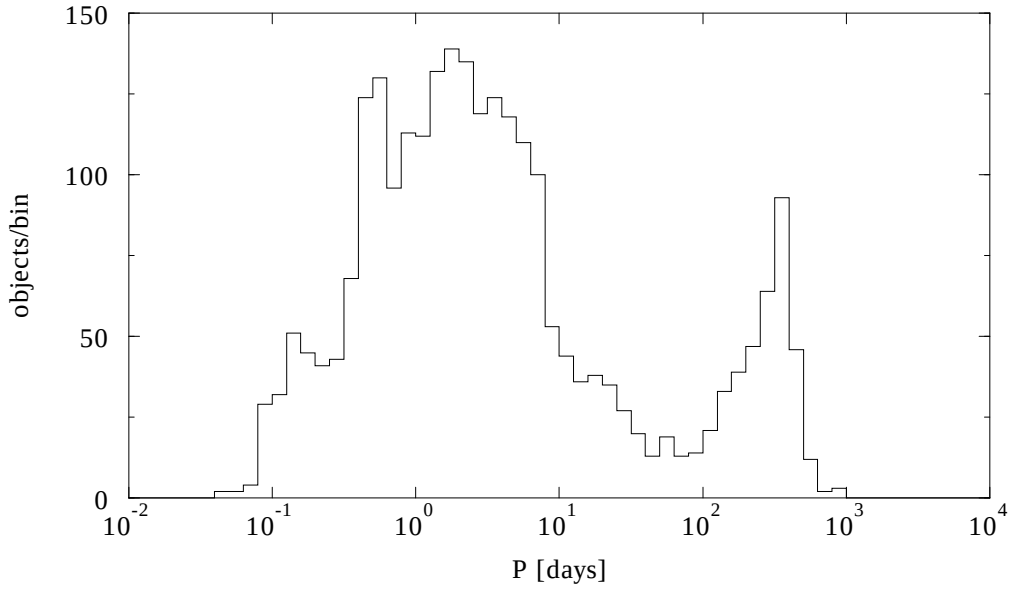

Figure 3.2.97. *Hipparcos Catalogue, Field H51: variability period, P (bin size $10^{0.1}$).*

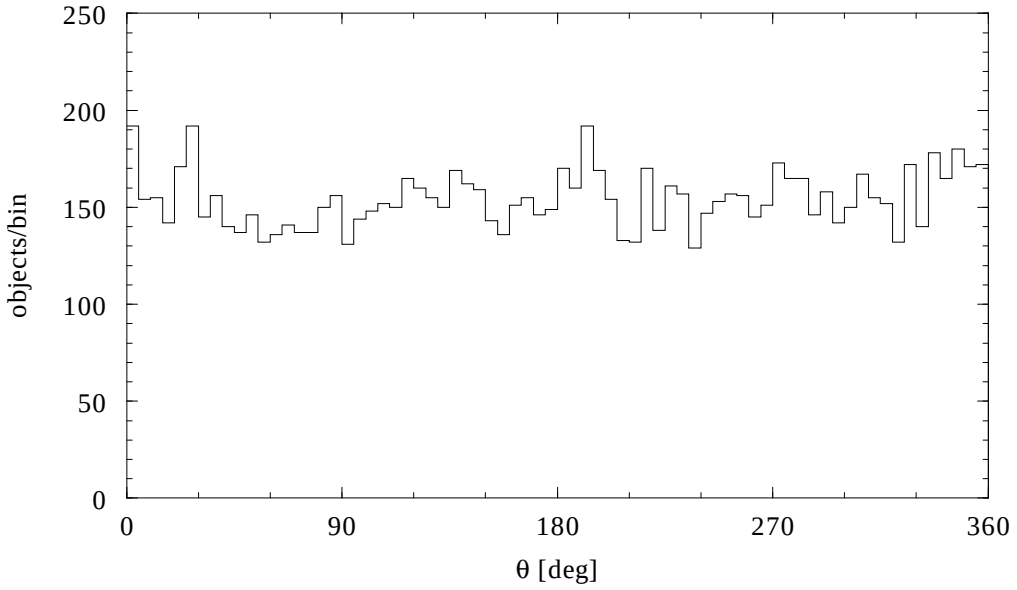

Figure 3.2.98. *Hipparcos Catalogue, Field H63: position angle, θ (bin size 5°).*

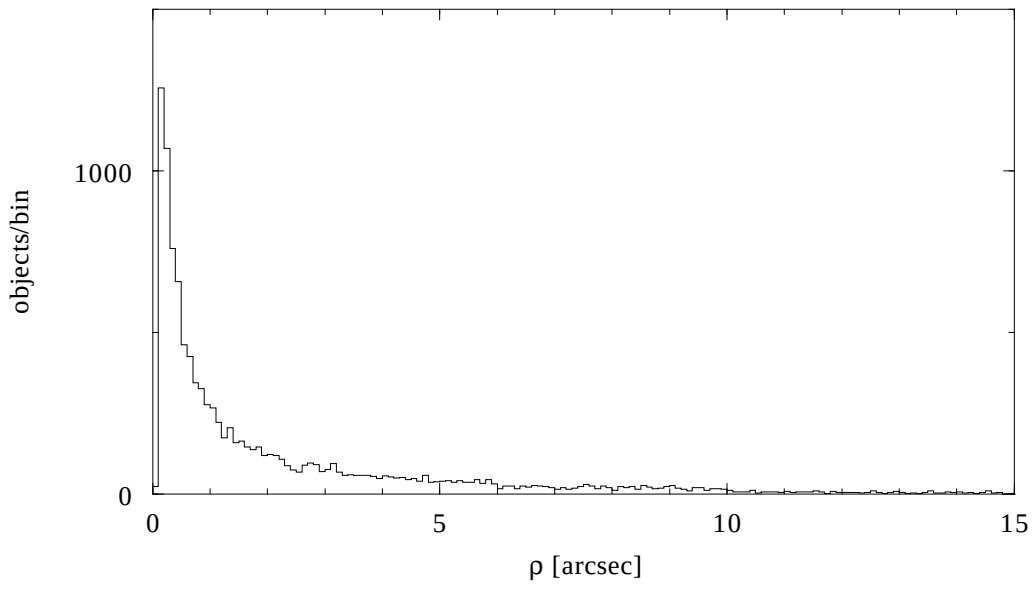

Figure 3.2.99. *Hipparcos Catalogue, Field H64: angular separation, ϱ (bin size 0.1 arcsec).*

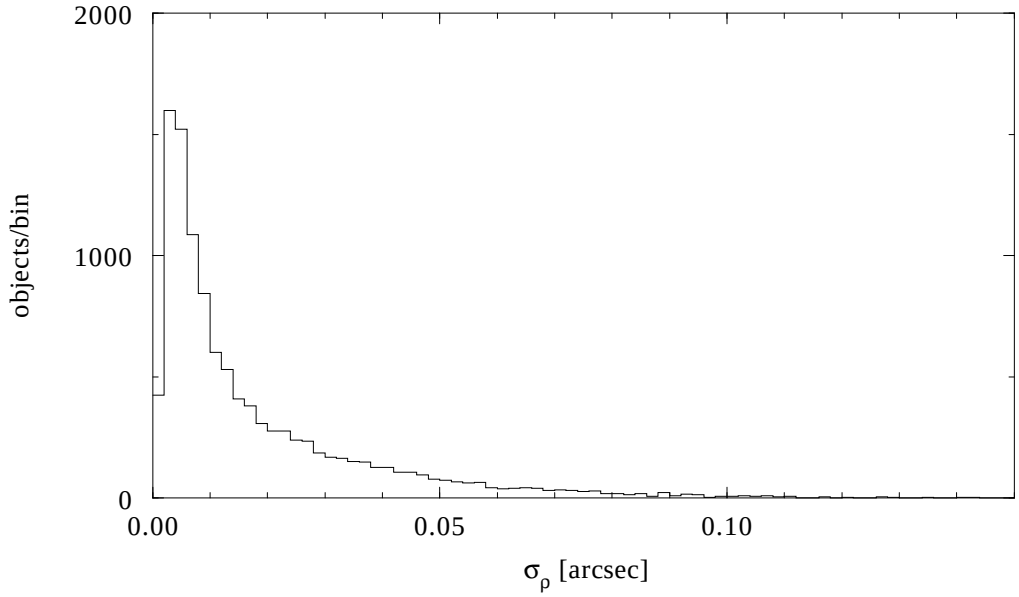

Figure 3.2.100. *Hipparcos Catalogue, Field H65: standard error in angular separation, ϱ (bin size 0.02 arcsec).*

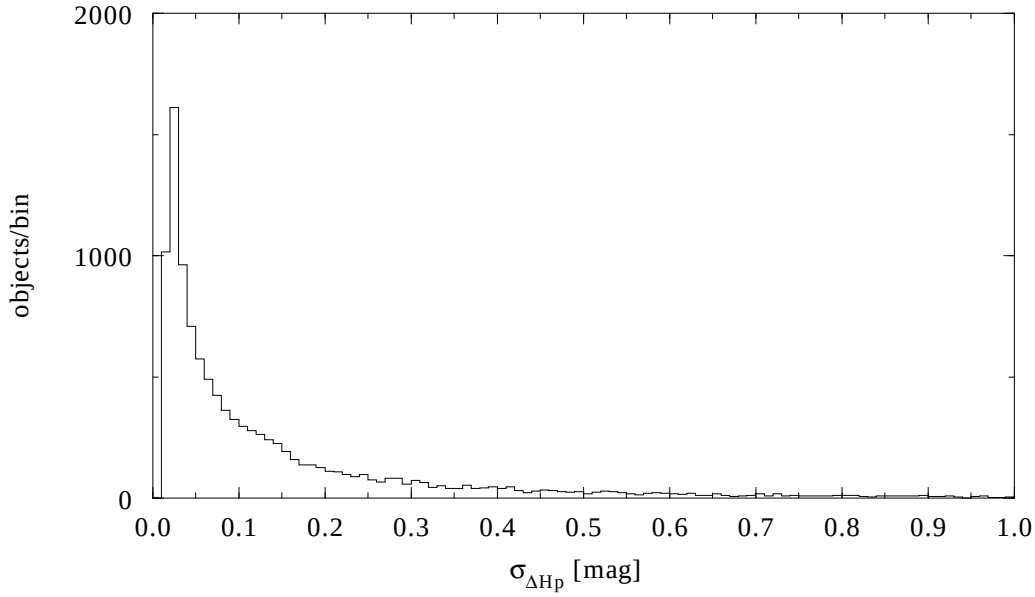

Figure 3.2.101. *Hipparcos Catalogue, Field H67: standard error in magnitude difference, ΔHp (bin size 0.01 mag).*

Figure 3.2.102. *Hipparcos Catalogue, Field H66: median magnitude difference, ΔHp, in galactic coordinates (cell size $2^\circ \times 2^\circ$). The distribution has been smoothed over the eight closest neighbours of each cell.*

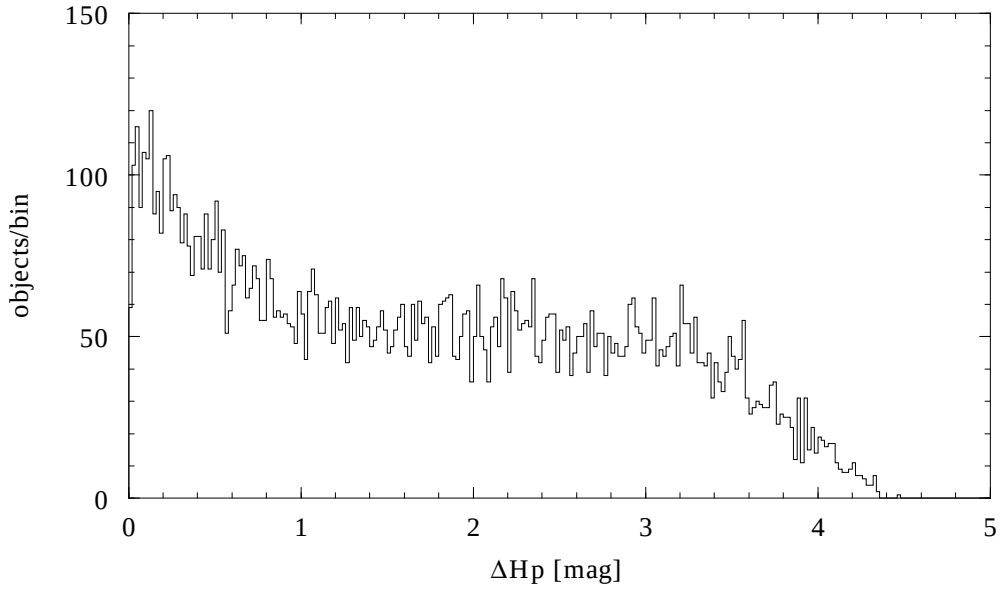

Figure 3.2.103. *Hipparcos Catalogue, Field H66: magnitude difference, ΔHp (bin size 0.02 mag).*

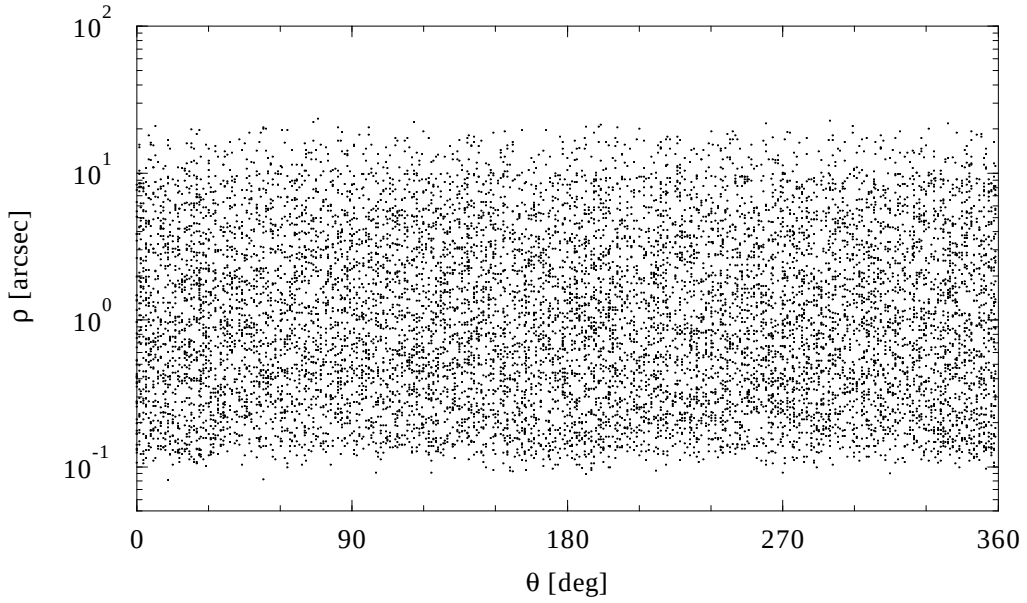

Figure 3.2.104. *Hipparcos Catalogue, Fields H63/H64: angular separation, ϱ versus position angle, θ.*

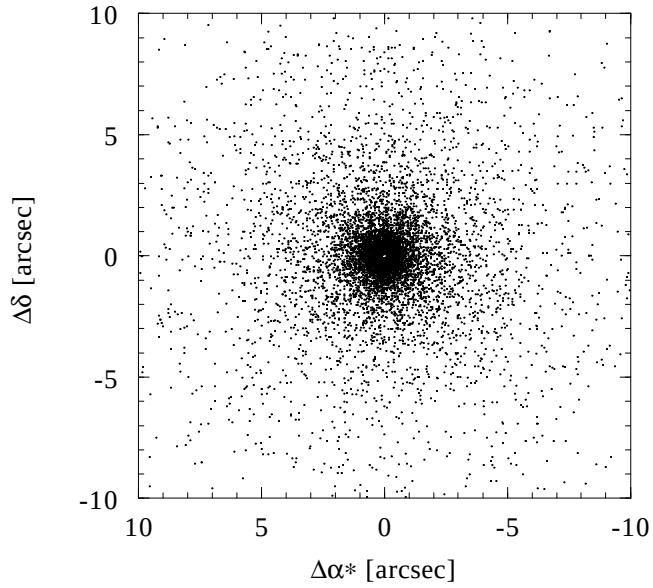

Figure 3.2.105. *Hipparcos Catalogue, Fields H63/H64: double star relative position from angular separation, ϱ, and position angle, θ.*

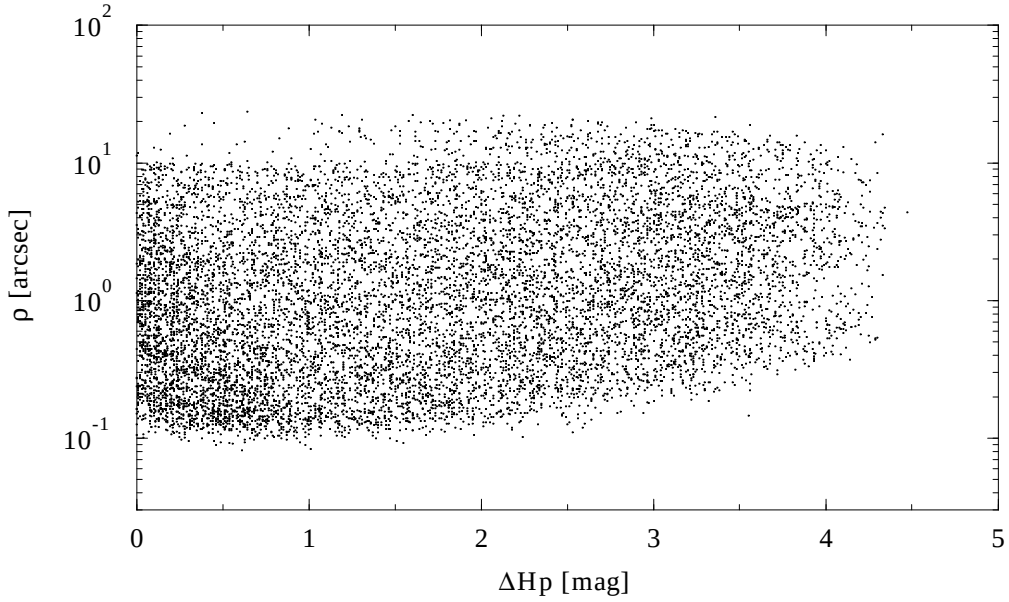

Figure 3.2.106. *Hipparcos Catalogue, Fields H63/H64: angular separation, ϱ versus magnitude difference, ΔHp.*

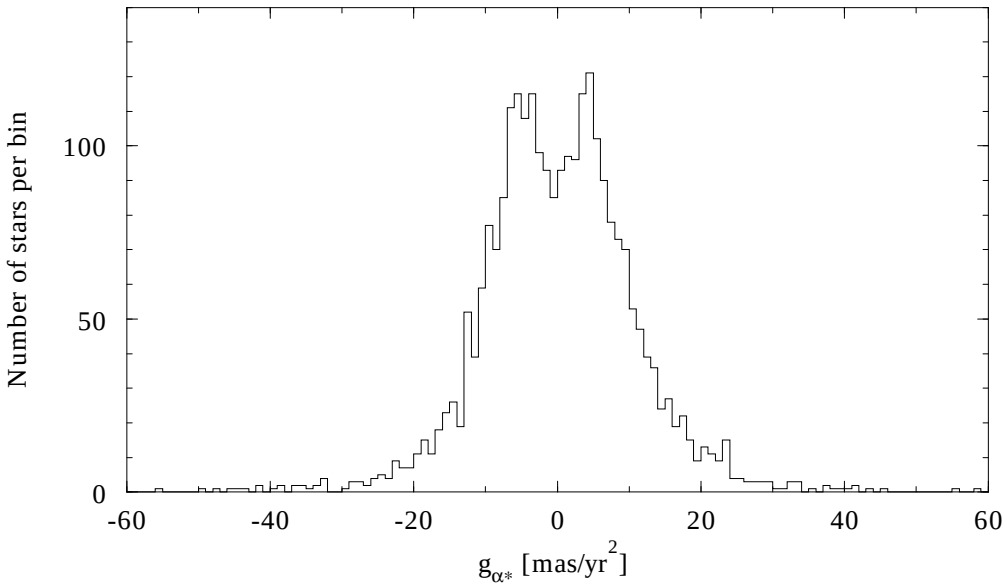

Figure 3.2.107. *Hipparcos Catalogue, DMSA/G, Field DG2: acceleration in right ascension at epoch J1991.25, $g_{\alpha*} = d\mu_{\alpha*}/dt$ (bin size 1 mas/yr^2).*

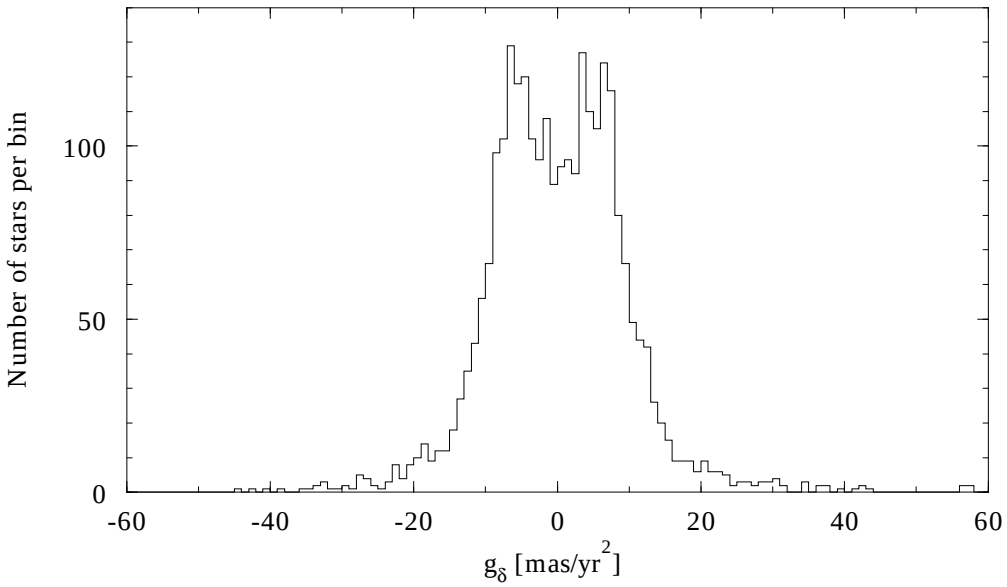

Figure 3.2.108. *Hipparcos Catalogue, DMSA/G, Field DG3: acceleration in declination at epoch J1991.25, $g_{\delta} = d\mu_{\delta}/dt$ (bin size 1 mas/yr^2).*

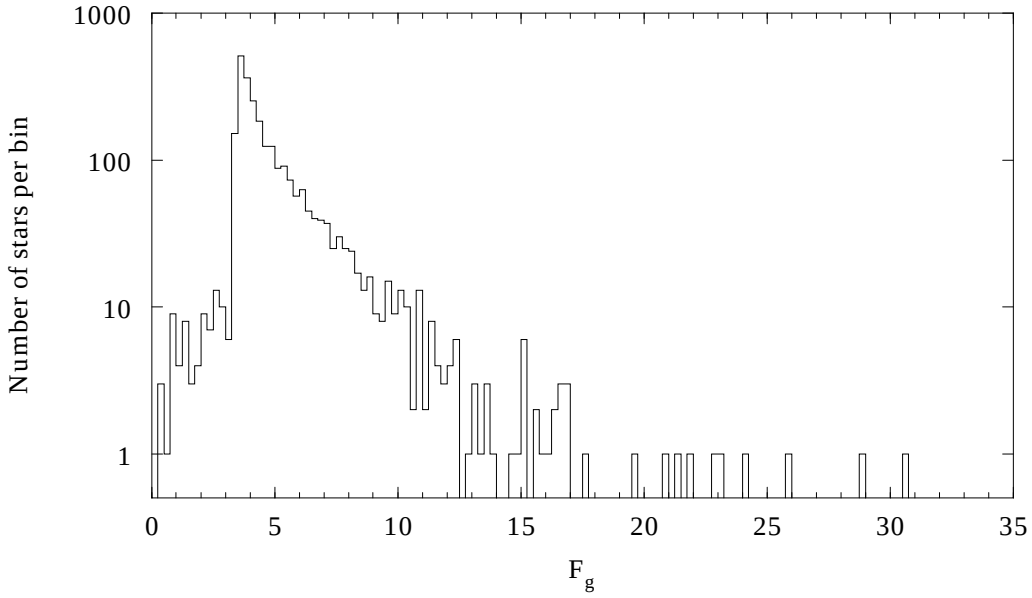

Figure 3.2.109. *Hipparcos Catalogue, DMSA/G, Field DG6: statistic for the significance of the accelerations, F_g (bin size 0.25).*

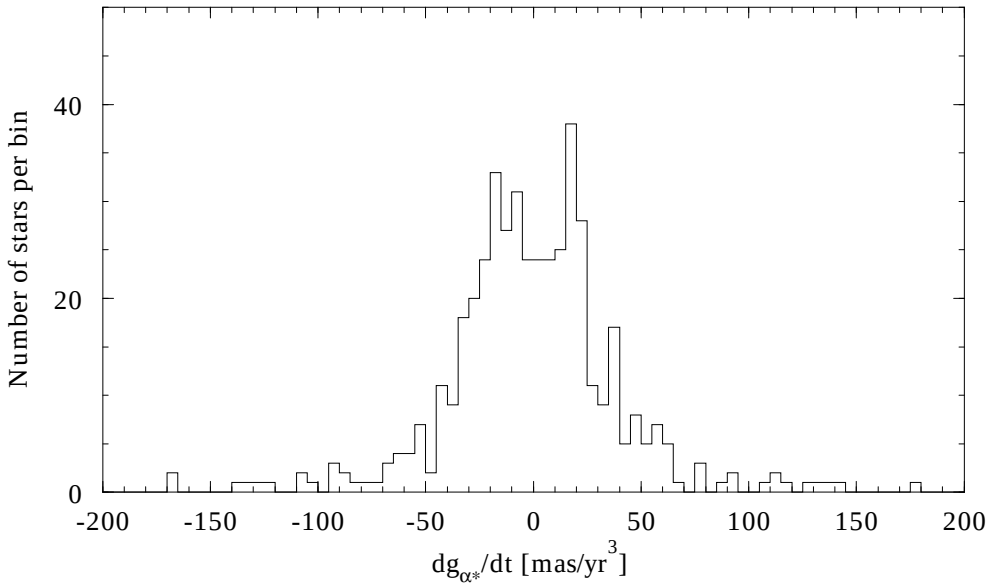

Figure 3.2.110. *Hipparcos Catalogue, DMSA/G, Field DG7: rate of change of $g_{\alpha*}$ at epoch J1991.25, $\dot{g}_{\alpha*} = d^2\mu_{\alpha*}/dt^2$ (bin size 5 mas/yr^3).*

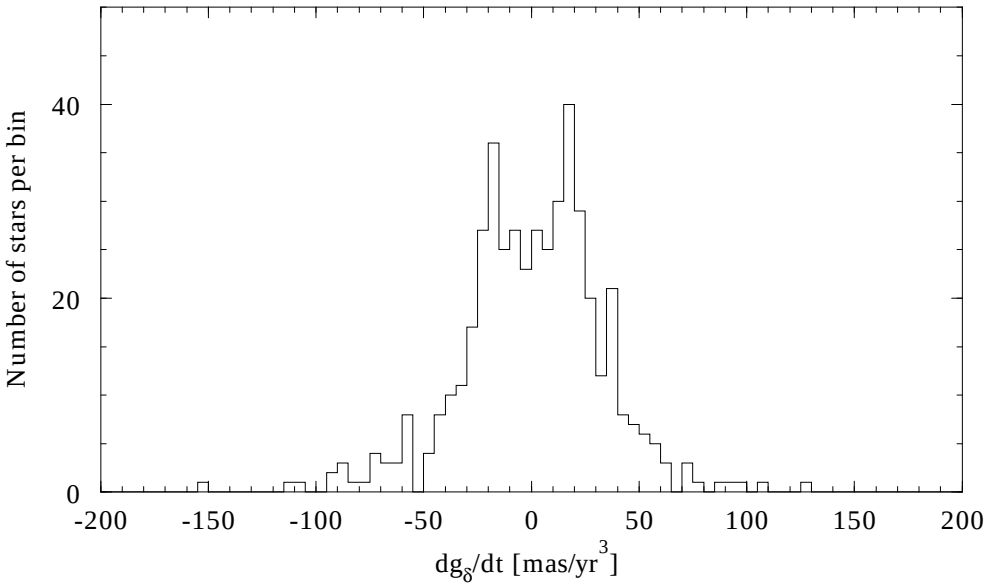

Figure 3.2.111. *Hipparcos Catalogue, DMSA/G, Field DG8: rate of change of g_δ at epoch J1991.25, $\dot{g}_\delta = d^2\mu_\delta/dt^2$ (bin size 5 mas/yr^3).*

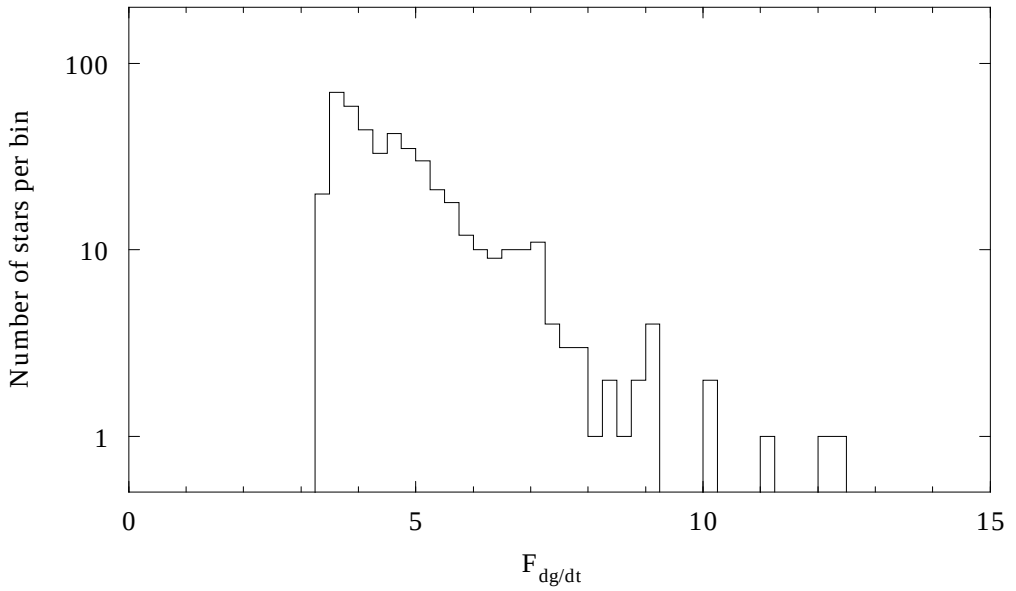

Figure 3.2.112. *Hipparcos Catalogue, DMSA/G, Field DG11: statistic for the significance of the rate of change of accelerations, $F_{\dot{g}}$ (bin size 0.25).*

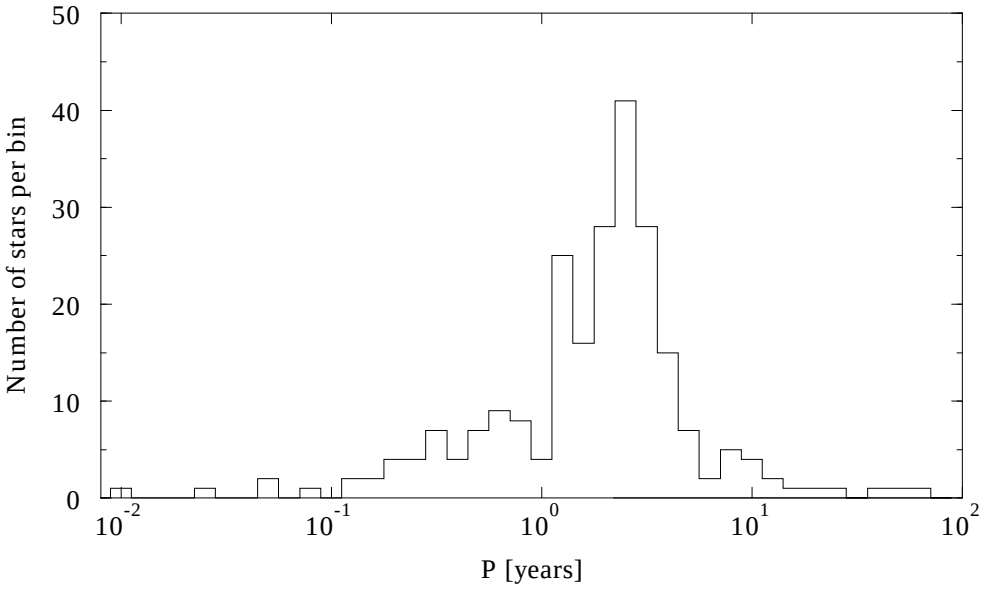

Figure 3.2.113. *Hipparcos Catalogue, DMSA/O, Field DO2: orbital period, P (bin size 0.1 dex).*

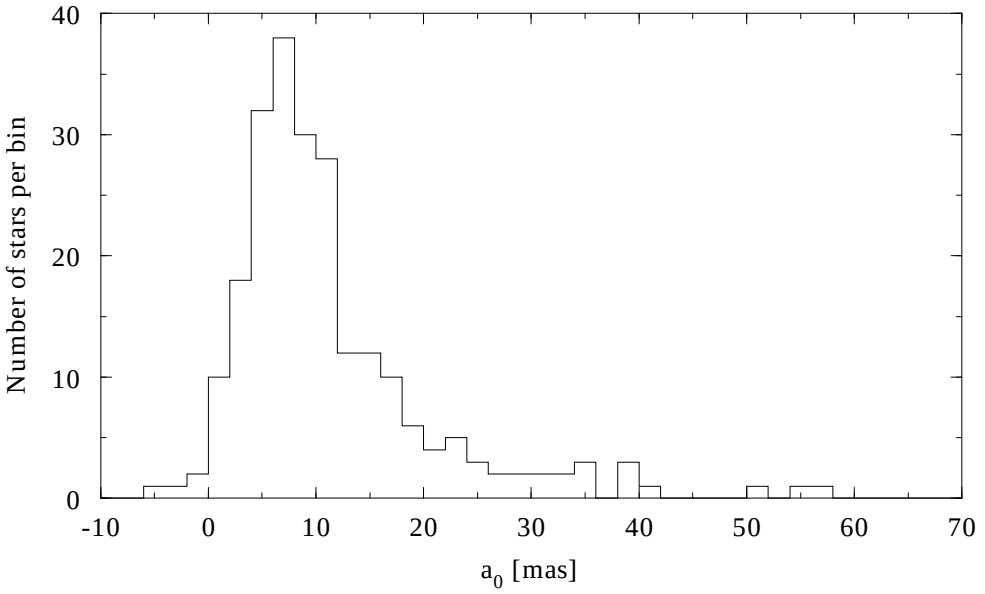

Figure 3.2.114. *Hipparcos Catalogue, DMSA/O, Field DO3: semi-major axis of the photocentre orbit, a_0 (bin size 2 mas).*

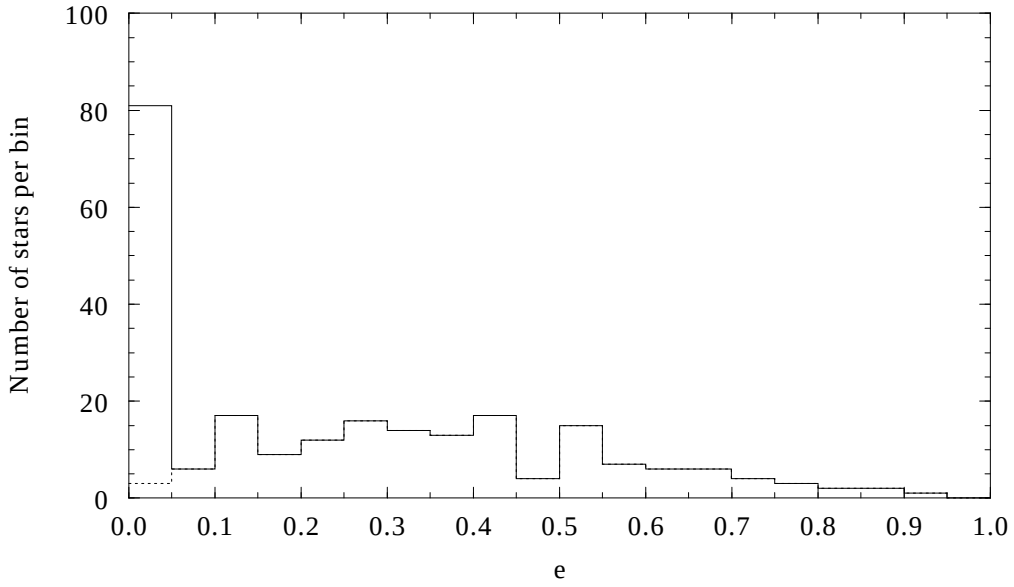

Figure 3.2.115. *Hipparcos Catalogue, DMSA/O, Field DO4: eccentricity, e (bin size 0.05). Solid line: all systems; dotted line: systems with assumed e = 0 and ω = 0 excluded.*

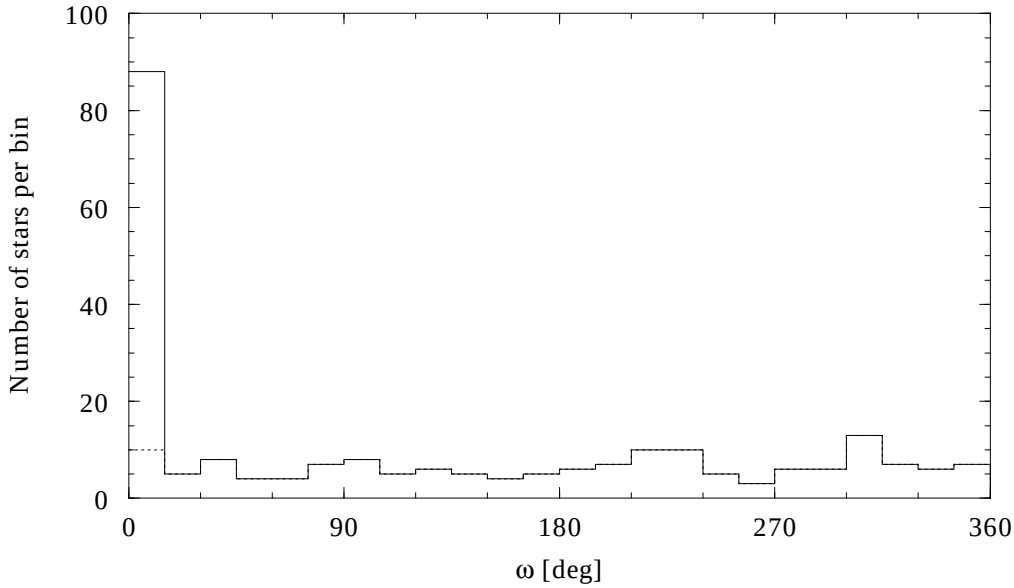

Figure 3.2.116. *Hipparcos Catalogue, DMSA/O, Field DO5: argument of periastron, ω (bin size 15°). Solid line: all systems; dotted line: systems with assumed e = 0 and ω = 0 excluded.*

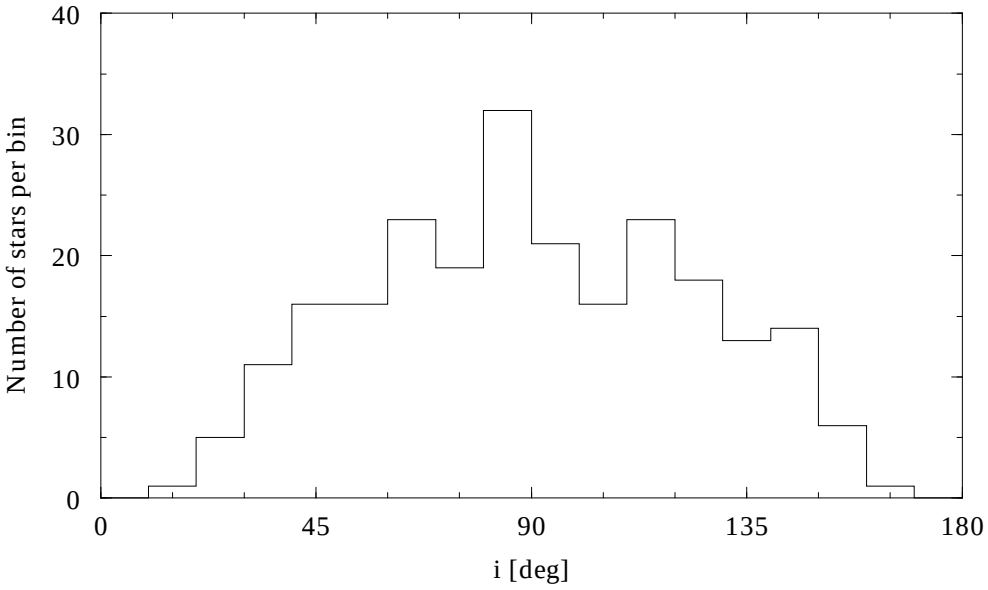

Figure 3.2.117. *Hipparcos Catalogue, DMSA/O, Field DO6: inclination, i (bin size 10°).*

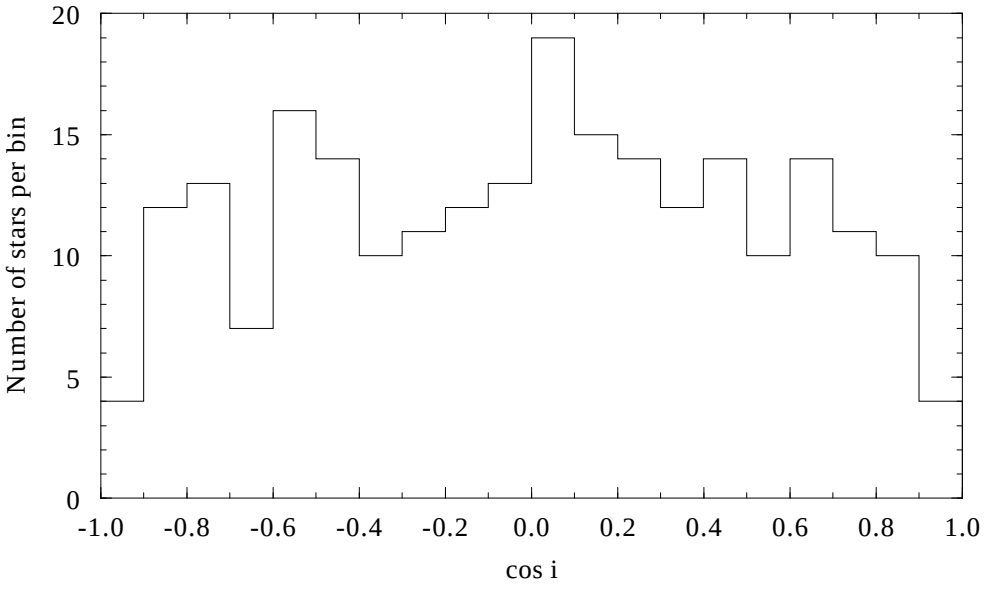

Figure 3.2.118. *Hipparcos Catalogue, DMSA/O, Field DO6: cosine of inclination, $\cos i$ (bin size 0.1).*

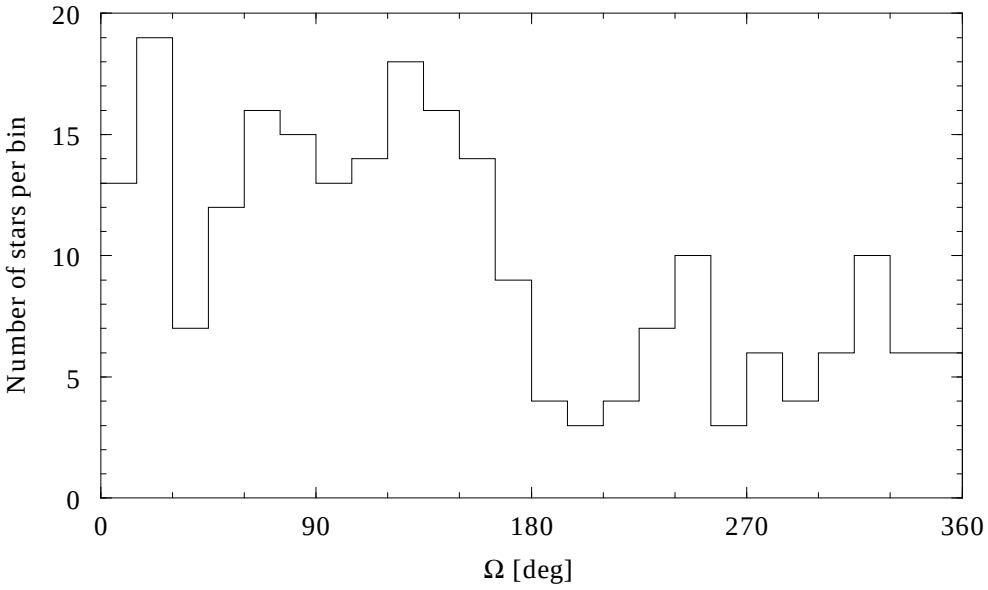

Figure 3.2.119. *Hipparcos Catalogue, DMSA/O, Field DO7: position angle of the node, Ω (bin size 15°).*

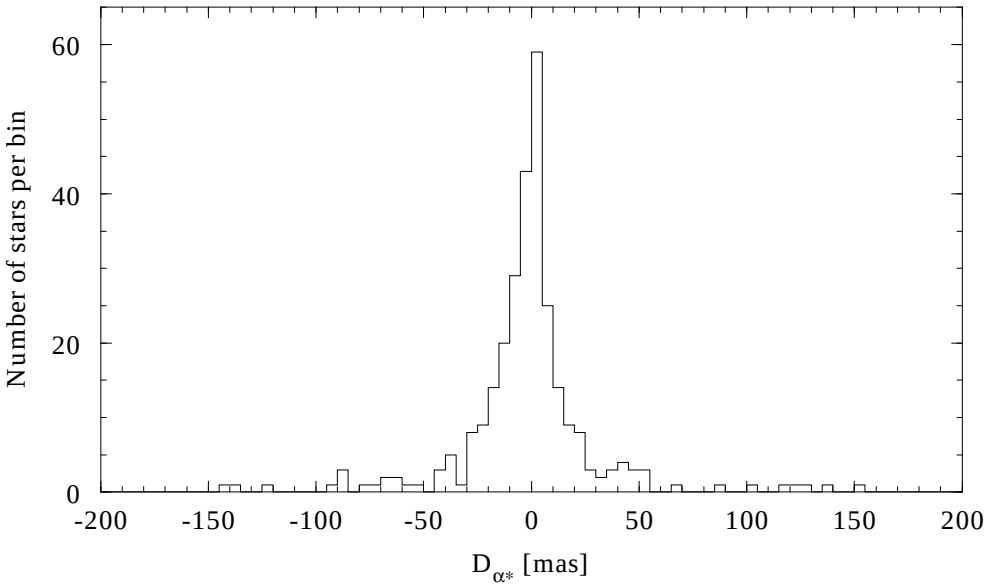

Figure 3.2.120. *Hipparcos Catalogue, DMSA/V, Field DV3: element of the variability-induced motion in right ascension, $D_{\alpha*}$ (bin size 5 mas).*

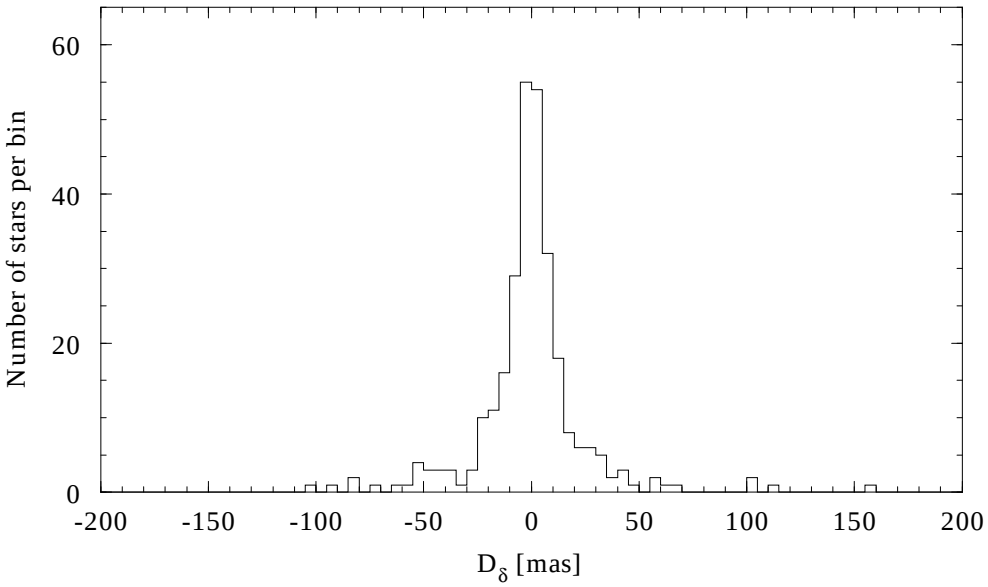

Figure 3.2.121. *Hipparcos Catalogue, DMSA/V, Field DV4: element of the variability-induced motion in declination, D_{δ} (bin size 5 mas).*

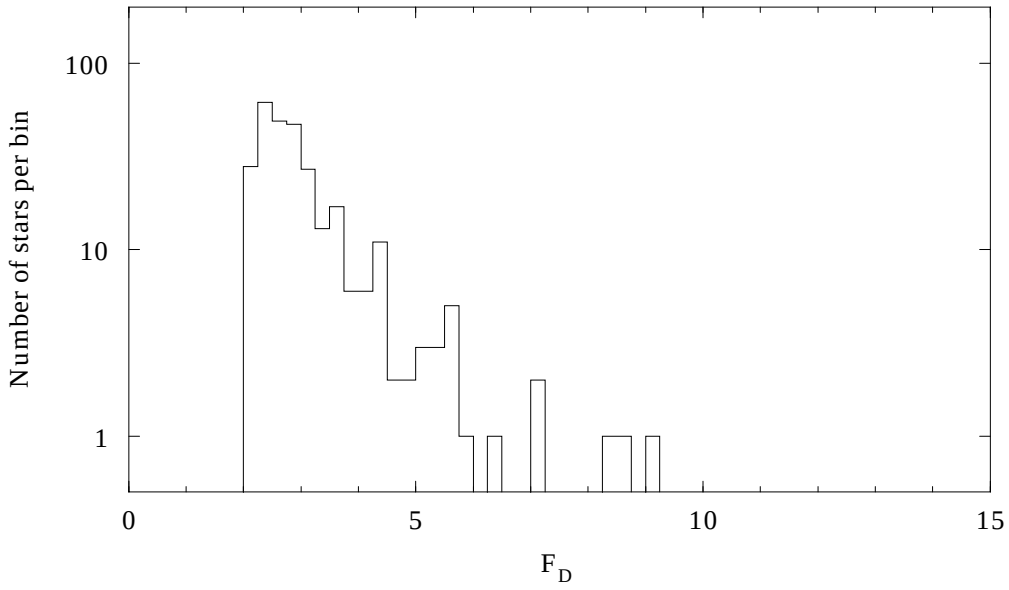

Figure 3.2.122. *Hipparcos Catalogue, DMSA/V, Field DV7: statistic for the significance of the variability-induced motion, F_D (bin size 0.25).*

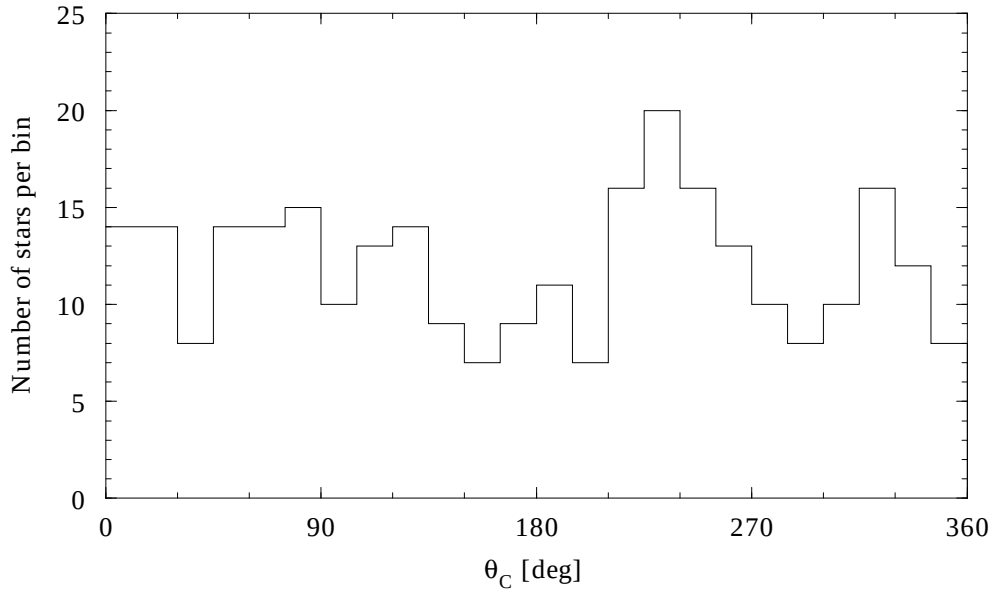

Figure 3.2.123. *Hipparcos Catalogue, DMSA/V, Field DV8: position angle of the constant component, θ_C (bin size 15°).*

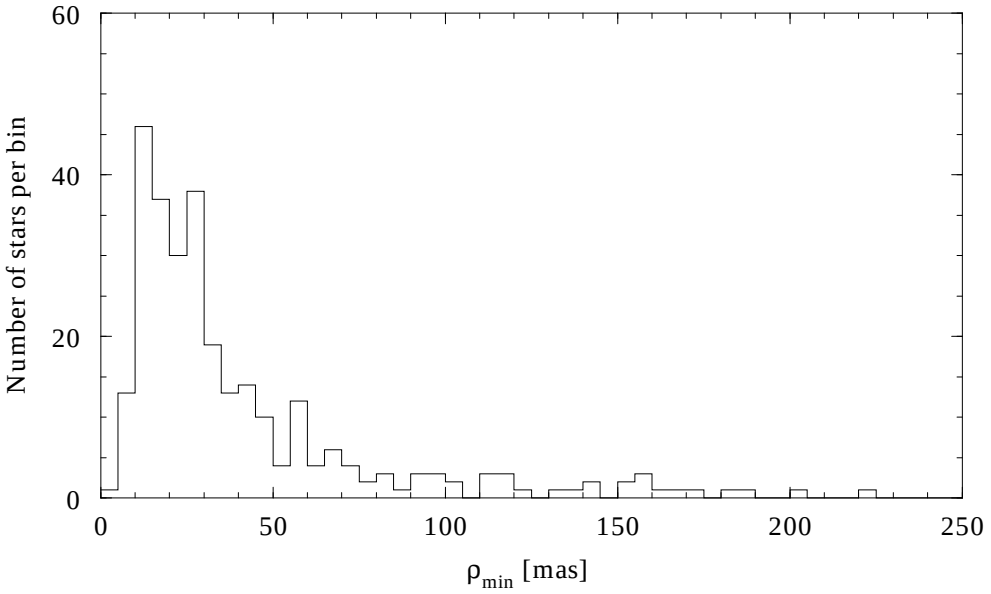

Figure 3.2.124. *Hipparcos Catalogue, DMSA/V, Field DV10: lower limit for the separation, ϱ_{min} (bin size 5 mas).*

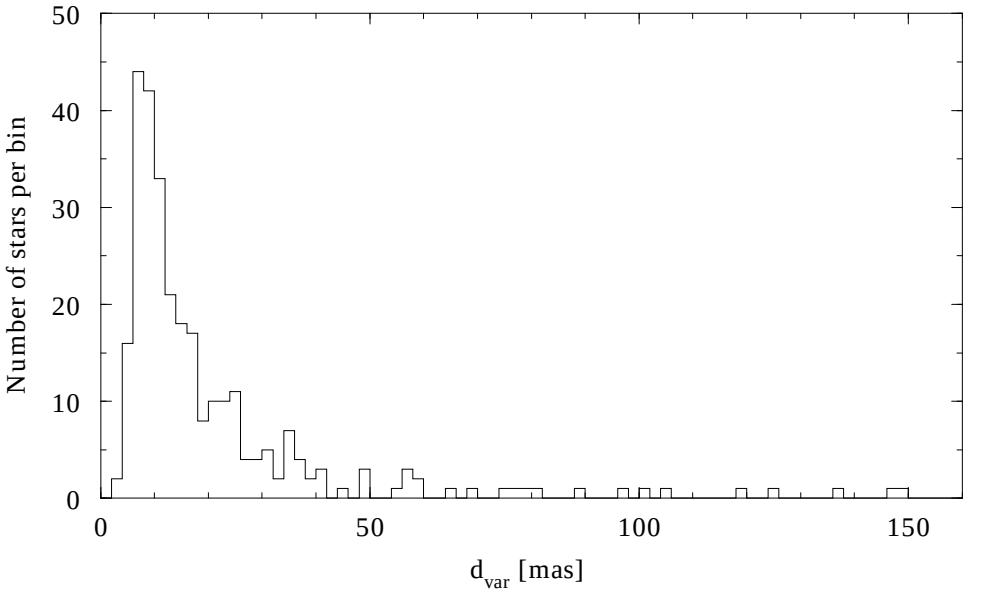

Figure 3.2.125. *Hipparcos Catalogue, DMSA/V, Field DV11: displacement of the photocentre between maximum and minimum luminosity, d_{var} (bin size 2 mas).*

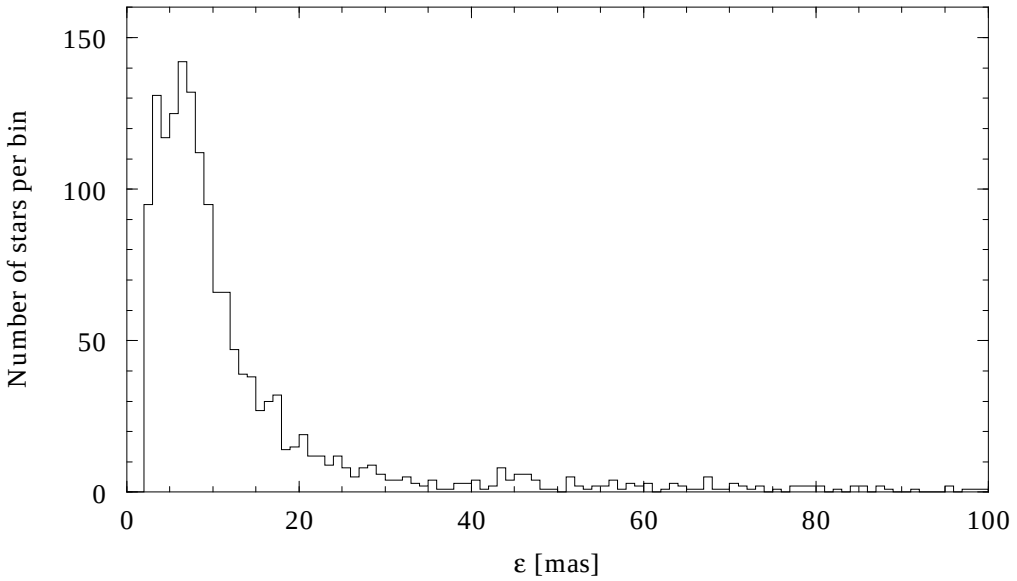

Figure 3.2.126. *Hipparcos Catalogue, DMSA/X, Field DX2: cosmic error, ϵ (bin size 1 mas).*

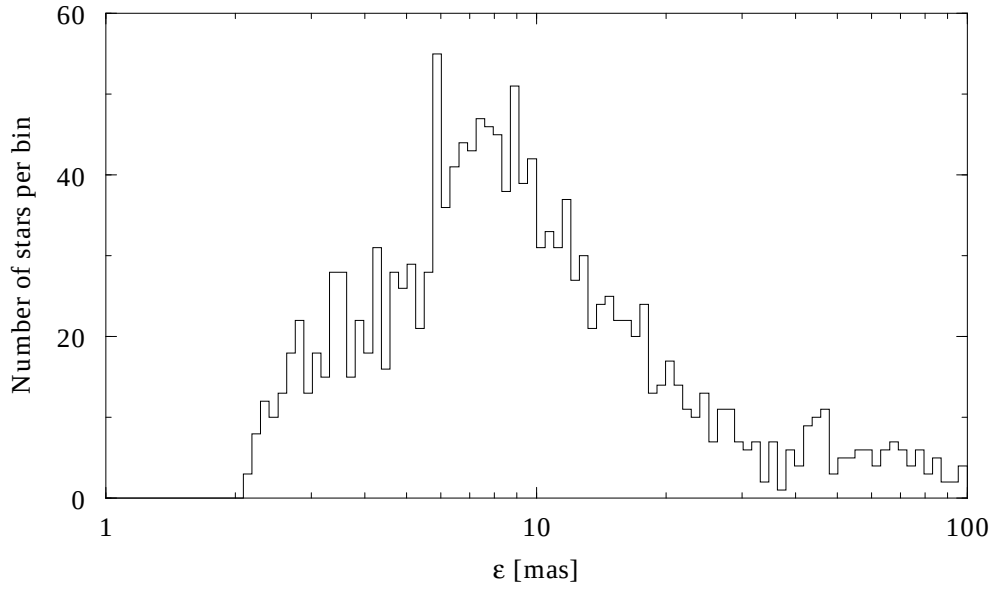

Figure 3.2.127. *Hipparcos Catalogue, DMSA/X, Field DX3: standard error in the cosmic error, σ_ϵ (bin size 0.02 dex).*